crystals

MDPI

Article

Synthesis and Crystal Structure of the Short $LnSb_2O_4Br$ Series (Ln = Eu–Tb) and Luminescence Properties of Eu^{3+}-Doped Samples

Felix C. Goerigk [1], Veronica Paterlini [2], Katharina V. Dorn [2], Anja-Verena Mudring [2,*] and Thomas Schleid [1,*]

1 Institute for Inorganic Chemistry, University of Stuttgart, Pfaffenwaldring 55, D-70569 Stuttgart, Germany; goerigk@iac.uni-stuttgart.de

2 Department of Materials and Environmental Chemistry, Arrhenius Laboratory, Stockholm University, S-10691 Stockholm, Sweden; veronica.paterlini@mmk.su.se (V.P.); katharina.dorn@mmk.su.se (K.V.D.)

* Correspondence: anja-verena.mudring@mmk.su.se (A.-V.M.); schleid@iac.uni-stuttgart.de (T.S.)

Received: 2 October 2020; Accepted: 23 November 2020; Published: 27 November 2020

Abstract: Pale yellow crystals of $LnSb_2O_4Br$ (Ln = Eu–Tb) were synthesized via high temperature solid-state reactions from antimony sesquioxide, the respective lanthanoid sesquioxides and tribromides. Single-crystal X-ray diffraction studies revealed a layered structure in the monoclinic space group $P2_1/c$. In contrast to hitherto reported quaternary lanthanoid(III) halide oxoantimonates(III), in $LnSb_2O_4Br$ the lanthanoid(III) cations are exclusively coordinated by oxygen atoms in the form of square hemiprisms. These $[LnO_8]^{13-}$ polyhedra form layers parallel to (100) by sharing common edges. All antimony(III) cations are coordinated by three oxygen atoms forming ψ^1-tetrahedral $[SbO_3]^{3-}$ units, which have oxygen atoms in common building up meandering strands along [001] according to $^1_\infty\{[SbO^v_{2/2}O^t_{1/1}]^-\}$ (v = vertex-sharing, t = terminal). The bromide anions are located between two layers of these parallel running oxoantimonate(III) strands and have no bonding contacts with the Ln^{3+} cations. Since Sb^{3+} is known to be an efficient sensitizer for Ln^{3+} emission, photoluminescence studies were carried out to characterize the optical properties and assess their suitability as light phosphors. Indeed, for both, $GdSb_2O_4Br$ and $TbSb_2O_4Br$ doped with about 1.0–1.5 at-% Eu^{3+} efficient sensitization of the Eu^{3+} emission could be detected. For $TbSb_2O_4Br$, in addition, a remarkably high energy transfer from Tb^{3+} to Eu^{3+} could be detected that leads to a substantially increased Eu^{3+} emission intensity, rendering it an efficient red light emitting material.

Keywords: lanthanoid compounds; halide oxoantimonates(III); structure elucidation; luminescence characterization; solid-state synthesis; single-crystal X-ray diffraction

1. Introduction

Lanthanoid compounds containing complex oxoanions are an interesting material class for application as light phosphors because the valence 4*f*-states of lanthanoids typically give rise to photoluminescence characteristic for the respective lanthanoid. However, direct photoexcitation into 4*f*-levels is an inefficient way to stimulate photoluminescence, because of the forbidden character of these transitions. For all-inorganic materials this problem can be circumvented through charge-transfer sensitization or by energy transfer (ET) from other metal cations, which are all allowed processes. Both processes are possible in lanthanoid(III) oxopnictogenates(III/V) [1–4], such as oxoantimonates, which are readily available through high-temperature solid-state reaction of the respective binary starting materials, i.e., the respective lanthanoid(III) and pnictogen(III) sesquioxides (Ln_2O_3 and Pn_2O_3). Moreover, the lanthanoid(III) oxoarsenates(III) or -antimonates(III) generally feature a quite high

stability in water and air. Varying the host lattice and the lanthanoid(III) dopant in these systems reveals the possibility to fine-tune the selective emission properties in a wide range [2,5,6]. For example, current research on Y[PO_4] co-doped with Gd^{3+} and Sb^{3+} revealed that antimon(III) cations are appropriate to activate gadolinium(III) emission in the ultraviolet (UV-B) range [7]. This inspired us to synthesize lanthanoid(III) containing oxoantimonates(III) to have materials at hand equipped with intrinsic Sb^{3+} cations as sensitizer for Ln^{3+} cations and therefore being suitable as efficient luminescent material class.

The structural diversity of lanthanoid(III) oxopnictogenates(III) is quite large and varies not only with the lanthanoid, but also on the pnictogen (As or Sb). Structural complexity can be enlarged through the incorporation of halide anions. For ternary lanthanoid(III) oxoarsenates(III) the compositions *Ln*AsO_3 (*Ln* = La, Ce) and $Ln_2As_4O_9$ (*Ln* = Pr, Nd, Sm) are known [8–11]. The *Ln*[AsO_3] representatives crystallize either with the α-Pb[SeO_3]- or the K[ClO_3]-type structure exhibiting coordination numbers of eight or nine for the lathanoid(III) cations and feature isolated ψ^1-tetrahedral $[AsO_3]^{3-}$ anions without any bridging As–O–As contacts as the dominating structural feature. These anions occur as discrete triangular pyramids with stereochemically active lone pairs at the As^{3+} cations. In contrast, the oxoarsenates $Ln_2As_4O_9$ display both $[As_2O_5]^{4-}$ pyroanions and cyclic $[As_4O_8]^{4-}$ units as condensation products of ψ^1-tetrahedral $[AsO_3]^{3-}$ entities according to $Ln_4[As_2O_5]_2[As_4O_8]$. Up to now, no other further ternary lanthanoid(III) oxoarsenates(III) are known.

The addition of fluxes, such as alkali-metal halides, to the oxide reaction mixtures in order to improve crystallization and reduce the reaction temperature often results in the formation of different halide-anion containing quaternary compounds, enriching the structural diversity. So far, three different compositions for lanthanide oxoarsenates(III) containing trivalent lanthanoids are known, i.e., $Ln_{5\times3}[AsO_3]_4$, $Ln_3OX[AsO_3]_2$ and $Ln_3X_2[As_2O_5][AsO_3]$. Similar to their halide-free congeners, they have in common ψ^1-tetrahedral $[AsO_3]^{3-}$ anions, and also feature pyroanionic $[As_2O_5]^{4-}$ groups. In contrast to them, because of the presence of halide anions, mixed oxide-halide coordination polyhedra around the Ln^{3+} cations occur, providing coordination numbers as high as seven, eight or nine [12–18].

With antimony as the heavier congener of arsenic, lanthanoid(III) oxoantimonates(III) with three different compositions are known: *Ln*Sb_5O_{12} (*Ln* = La), $Ln_3Sb_5O_{12}$ (*Ln* = Pr, Nd, Sm–Gd and Yb) and *Ln*SbO_3 (*Ln* = Ce). While $LaSb_5O_{12}$ contains both Sb^{3+} and Sb^{5+} cations with coordination numbers of three and six, respectively, featuring pyramidal $[SbO_3]^{3-}$ as well as octahedral $[SbO_6]^{7-}$ anions, $Ln_3Sb_5O_{12}$ and $CeSbO_3$ include antimony(III) cations exclusively. In the $Ln_3Sb_5O_{12}$ series, coordination numbers of three and four for the Sb^{3+} cations with oxygen atoms are present in the shape of vertex-connected $[SbO_3]^{3-}$ ψ^1-tetrahedra and $[SbO_4]^{5-}$ ψ^1-square pyramids, while the unique central lanthanoid(III) cation is coordinated eightfold by oxygen atoms. In cubic $CeSbO_3$, coordination numbers of 8 for cerium and 6 for antimony are reported with identical interatomic distances (d(Ce-O) = d(Sb-O) = 234 pm). However, both crystallographically independent oxygen-atom sites have to be only occupied by about 85% to realize trivalent antimony, so the true crystal structure of $CeSbO_3$ remains puzzling [19–23].

Compared to the oxoarsenates(III), analogous compounds with the heavier congener antimony synthesized under halide-flux conditions seemed to be restricted to the formula type $Ln_5X_3[SbO_3]_4$ (tetragonal, *P*4/*ncc* for *X* = F; monoclinic, *P*2/*c* for *X* = Cl) [24,25]. For the heavier lanthanoids, divergent oxoantimonate(III) halides with the composition *Ln*Sb_2O_4X are encountered, which exhibit completely different structural features in their crystal structures known so far and can be interpreted as derivatives of the rare-earth metal(III) (*RE*) oxobismuthate(III) halides (*RE*Bi_2O_4X with *RE* = Y, Pr, Nd and Sm-Lu for *X* = Cl-I) [26–29]. For lanthanum being the largest rare-earth metal(III) cation, an antimony(III)- and bromide-containing crystal structure with the formula $(La_{0.75}Sb_{0.25})OBr$ related to LaOBr (PbFCl-type structure, tetragonal, *P*4/*nmm*) is also reported, which can be understood as heavily Sb^{3+}-doped LaOBr [25]. Not in this compound, but in all the *Ln*Sb_2O_4X cases, the Ln^{3+} cations have only contact to oxygen atoms resulting in square $[LnO_8]^{13-}$ square prisms. In $Ln_{1+n}Sb_{2-n}O_4X$ with *Ln* = Nd, Sm and *X* = Cl, Br as the only known members, tetragonal crystal structures (*P*4/*mmm*) containing anionic layers of vertex-sharing square pyramidal $[SbO_4]^{5-}$ units (square ψ^1-pyramids) according to ${}^2_\infty\{[SbO^v_{4/2}]^-\}$

(v = vertex-sharing) are observed. The halide anions have little or no contact to the Ln^{3+} cations, but settle with far away Sb^{3+} cations at positions, where four of them encircle their stereochemically active lone pairs. However, no knowledge of further representatives and their crystal structures for the heavier lanthanoid(III) systems *Ln*-Sb-O-*X* was available up to now.

In this work, we report on the single-crystal synthesis of the short $LnSb_2O_4Br$ series (*Ln* = Eu–Tb) crystallizing in a novel structure type featuring layered polyhedra around the central lanthanoid(III) cations without any contact to the bromide anions. With the crystal structure at hand, photoluminescence measurements of bulk $GdSb_2O_4Br$ were performed to investigate the luminescence processes caused by Sb^{3+}. With this understanding, the photoluminescence investigations of $EuSb_2O_4Br$ and $TbSb_2O_4Br$ as well as doped $GdSb_2O_4Br:Eu^{3+}$ and $TbSb_2O_4Br:Eu^{3+}$ were undertaken to examine the consequence of incorporating multiple luminescent cations. The article discusses both the relevant excitation and emission spectra and deals with possible energy transfer mechanisms of the involved ions investigated with lifetime measurements to reach an understanding about the major luminescence processes taking place and the special role of Sb^{3+} cations in the crystal structure as intrinsic sensitizers and possible efficient alternative to the forbidden direct excitation via 4*f*-4*f* transitions of the Ln^{3+} ions.

2. Materials and Methods

2.1. Synthesis of $LnSb_2O_4Br$ Representatives

The lanthanoid(III) oxoantimonate(III) bromides $LnSb_2O_4Br$ (*Ln* = Eu–Tb) were synthesized via solid-state reactions from sesquioxides with anhydrous lanthanide tribromides (Ln_2O_3: ChemPur, Karlsruhe, Germany, 99.9%) at elevated temperatures. About 1.0 mg (0.0028 mmol) of Eu_2O_3 was applied for doping and 54 mg (0.154 mmol) for the pure europium compound, gadolinium sesquioxide (Gd_2O_3: 54 mg, 0.153 mmol) or in case of *Ln* = Tb a mixture of terbium metal (Tb: ChemPur, Karlsruhe, Germany, 99.9%: 8 mg, 0.050 mmol) and terbium(III,IV) oxide (Tb_4O_7: ChemPur, Karlsruhe, Germany, 99.9%: 49 mg, 0.066 mmol) for in-situ synproportionation of Tb_2O_3, lanthanoid(III) tribromide ($EuBr_3$, $GdBr_3$ and $TbBr_3$, Sigma-Aldrich, Taufkirchen, Germany, 99.99%: 61 mg, 0.153 mmol) and antimony sesquioxide (Sb_2O_3: ChemPur, Karlsruhe, Germany, 99.9%: 134 mg, 0.460 mmol) served as starting materials according to Equation (1). Eutectic mixtures of cesium bromide (CsBr: ChemPur, Karlsruhe, Germany, 99.9%: 530 mg, 2.490 mmol) and sodium bromide (NaBr: Merck, Darmstadt, Germany, suprapur: 127 mg, 1.234 mmol) were used as flux.

$$Ln_2O_3 + LnBr_3 + 3\,Sb_2O_3 \xrightarrow{CsBr + NaBr} 3\,LnSb_2O_4Br\ (Ln = EuTb) \quad (1)$$

The reactions were carried out in evacuated fused silica ampoules (Quarz- und Glasbläserei Müller, Berlin-Adlershof, Germany; inner diameter: 10 mm, wall thickness: 1 mm, length: 60 mm). The starting materials were transferred into the ampoules inside of an argon-filled glove box (Glovebox Systemtechnik, GS Mega E-Line, Malsch, Germany) and sealed under dynamic vacuum. The multi-stage heating program shown in Figure A1 was applied employing a Nabertherm L 9/12 muffle furnace (Nabertherm, Lilienthal, Germany). Generally, cooling rates of 2–3 °C h^{-1} were chosen. An increase of the rates to 5 °C h^{-1} upwards resulted in a significant decrease of the obtained crystal size.

After cooling to room temperature, the samples were washed with about 250 mL demineralized water and dried subsequently in a drying oven at 80 °C for at least 6 h. First visual inspection with a stereo microscope of the powder samples revealed a homogeneous, pale yellow powder with square tabular shaped crystals of the target compound. However, using crossed-polarized light indicated the tendency for the formation of aggregated and twinned crystals.

2.2. Single-Crystal and Powder X-ray Diffraction

For single-crystal X-ray diffraction (SCXRD) measurements, crystals of adequate size were isolated under a stereomicroscope and fixed with grease into a glass capillary (outer diameter: 0.1 mm, wall

thickness: 0.01 mm). The diffraction experiments were performed on a Stoe StadiVari four-circle diffractometer (Stoe and Cie, Darmstadt, Germany) with Eulerian cradle and Mo-K_α radiation at room temperature. For data collection and integration, Stoe X-Area 1.86 (2018) was used [30]. The crystal structures of $EuSb_2O_4Br$ and $TbSb_2O_4Br$ were solved in the space group $P2_1/c$ through direct methods and subsequently refined using the ShelX-1997 program package [31,32].

Powder X-ray diffraction (PXRD) experiments were performed on a Stoe Stadi-P diffractometer with monochromatic Cu-K_α radiation (λ = 154.06 pm) in transmission geometry and a Stoe linear PSD detector with a range of 5°/2θ. As monochromator, a curved germanium single crystal with (111) as diffractive face was used. About 5 mg of the slightly crushed sample were fixed between two layers of an amorphous adhesion tape.

Since it was not possible to grow single crystals of $GdSb_2O_4Br$ in sufficient quality for single-crystal X-ray diffraction analysis, a Le Bail profile fit of the powder data for $GdSb_2O_4Br$ to obtain the lattice constants with the Fullprof suite was performed [33–36]. $EuSb_2O_4Br$ was used as the starting model.

2.3. Electron-Beam Microprobe Analysis

Scanning electron images as well as energy- and wavelength-dispersive X-ray spectrometry were performed on a Cameca SX-100 microanalyzer (Cameca, Gennevilliers, France) equipped with one energy-dispersive X-ray spectrometer (EDXS, ThermoScientific UltraDry, Waltham, MA, USA) and five wavelength-dispersive X-ray spectrometers (WDXS). Crystals of sufficient size were placed on a conductive carbon pad (Plano G3357, Wetzlar, Germany) and afterwards coated with a thin carbon layer to prevent surface charging. An acceleration voltage of 20 kV was chosen to improve the intensities of the emission lines of the heavier elements. Quantification of an europium(III)-doped sample of $TbSb_2O_4Br$ was performed by using Eu[PO_4], Tb[PO_4], InSb and CsBr for instrument calibration. The oxygen content was calculated using the individual valences of all present ions. As matrix correction, the Pouchou and Pichoir algorithm "PaP" as implemented in the Cameca PeakSight 6.2 package was applied [37–39].

2.4. Photoluminescence Investigations

Photoluminescence measurements were carried out at room temperature on a Fluorolog-3 modular spectrofluorometer (Horiba JobinYvon, France), equipped with a double excitation monochromator, a single emission monochromator (HR320), and a R928P PMT detector. A continuous xenon lamp (450 W) was used as the excitation source for steady state measurements. For lifetime acquisition, the time-correlated single photon counting (TCSPC) technique was used, with a xenon microsecond-pulsed lamp for excitation. For both steady state and lifetimes measurements, the samples were measured as powders in front field geometry, by putting the sample holder plane perpendicular to the incoming ray, and collecting the emitted light at 22.5° from the incident light.

3. Results and Discussion

3.1. Crystal-Structure Description

All members of the $LnSb_2O_4Br$ series (*Ln* = Eu–Tb) crystallize in the monoclinic space group $P2_1/c$ with four formula units per unit cell. The lanthanoid(III) cations (Ln^{3+}) occupy only one crystallographically unique position exhibiting a coordination number of eight. Being coordinated exclusively by oxygen atoms, distorted $[LnO_8]^{13-}$ anti- or hemiprisms are formed (Figure 1). The observed lanthanoid(III)-oxygen bond lengths fall into the range between 227 and 258 pm, which are similar to those found in the respective sesquioxides (Eu_2O_3 (Sm_2O_3- or B-type: 224–262 pm and bixbyite- or C-type: 230–239 pm), Gd_2O_3 (Sm_2O_3- or B-type: 215–270 pm and bixbyite- or C-type: 228–239 pm) and Tb_2O_3 (Sm_2O_3- or B-type: 218–273 pm and bixbyite- or C-Type: 227–239 pm) [40–45]. These $[LnO_8]^{13-}$ polyhedra are edge-connected by common oxygen atoms

to form infinite layers spreading out parallel to the (100) plane according to the Niggli formula $^{2}_{\infty}\{[LnO^{e}_{8/2}]^{5-}\}$ (e = edge-sharing, Figure 2).

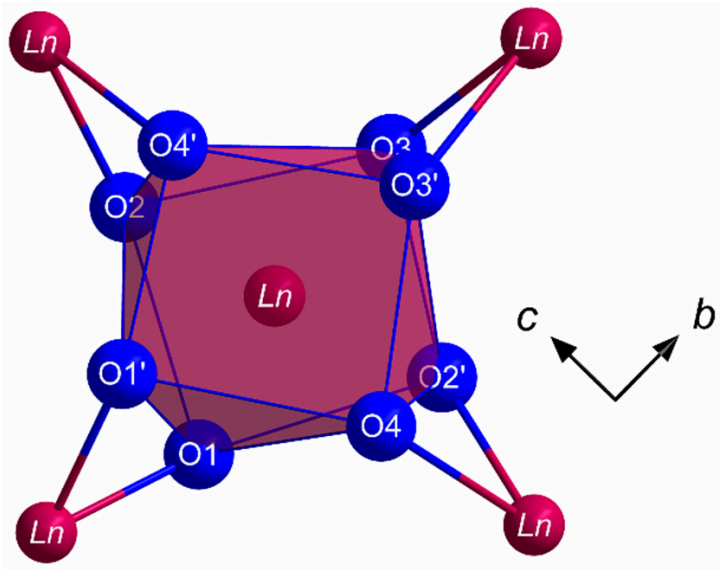

Figure 1. Coordination sphere of the Ln^{3+} cations in the crystal structure of the $LnSb_2O_4Br$ series (Ln = Eu–Tb) built up by eight oxygen atoms in the shape of a square $[LnO_8]^{13-}$ hemiprism.

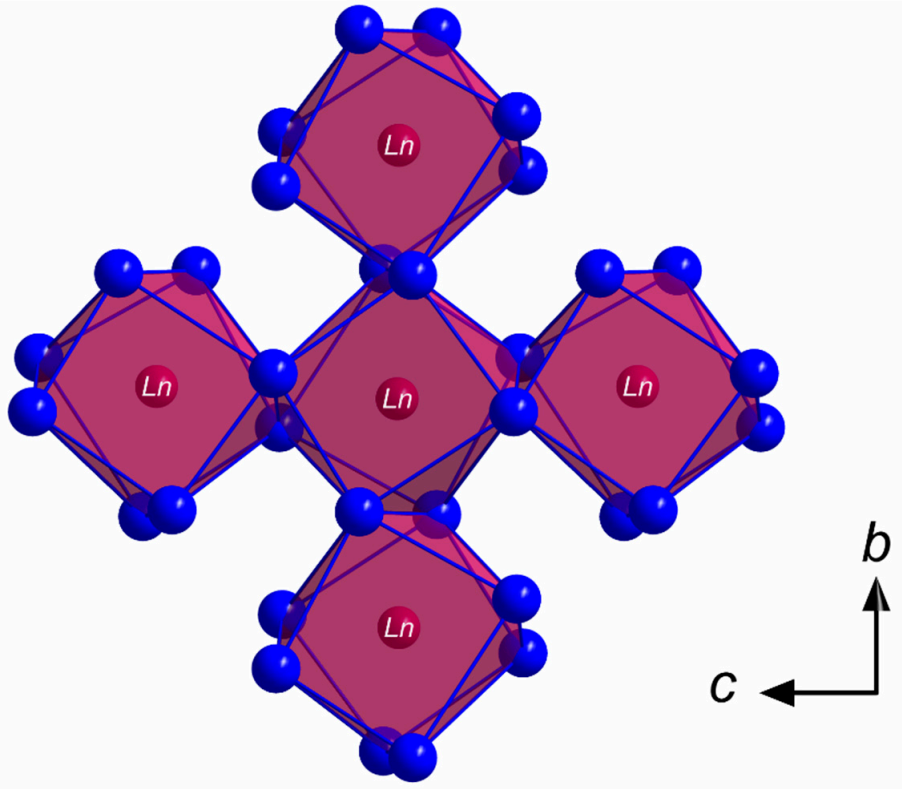

Figure 2. Infinite layer of the composition $^{2}_{\infty}\{[LnO^{e}_{8/2}]^{5-}\}$ in the crystal structure of the $LnSb_2O_4Br$ series (Ln = Eu–Tb) as viewed along [100] showing edge-connected $[LnO_8]^{13-}$ hemiprisms spreading out parallel to the (100) plane.

The Sb^{3+} cations occupy two different crystallographic positions. Both $(Sb1)^{3+}$ and $(Sb2)^{3+}$ are surrounded by three oxygen atoms each in the shape of $[SbO_3]^{3-}$ ψ^1-tetrahedra (Figure 3). These pyramidal units share common oxygen atoms and build up infinite strands of vertex-connected $[SbO_3]^{3-}$ ψ^1-tetrahedra with alternating $(Sb1)^{3+}$ and $(Sb2)^{3+}$ cations meandering along the *c* axis (Figure 4) according to $^1_\infty\{[SbO^v_{2/2}O^t_{1/1}]^-\}$ (v = vertex-sharing, t = terminal). The different bonding situation is also reflected well by the interatomic Sb^{3+}–O^{2-} distances. While the terminal oxygen atoms reside at distances of about 193 pm to the central Sb^{3+} cations, the linking ones exhibit noticeable longer values with 205–212 pm. These different values are also illustrated in Figure 4 for the example of $TbSb_2O_4Br$ and all lone pairs present at the Sb^{3+} cations are pointing into the same direction along [100].

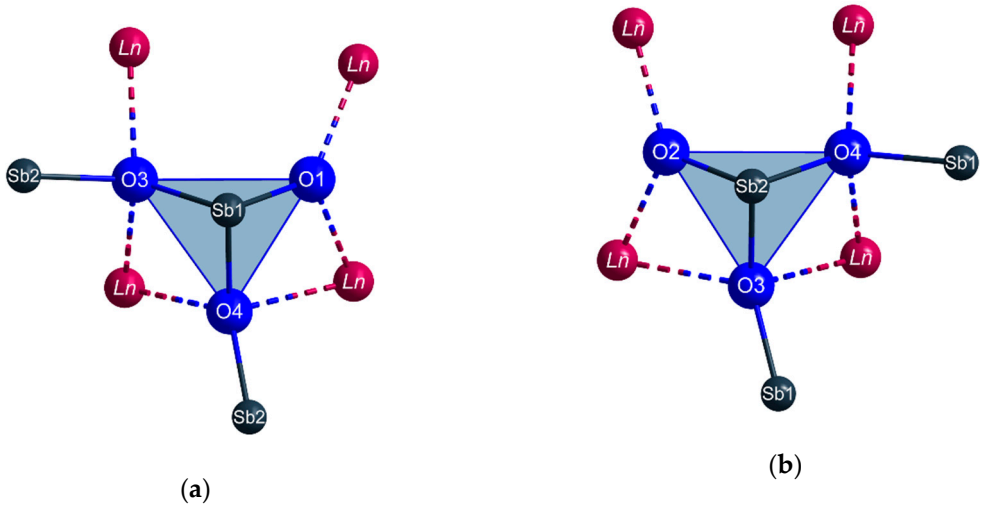

Figure 3. The first and second coordination spheres of the two crystallographically different Sb^{3+} cations (**a**): Sb1, (**b**): Sb2) in the crystal structure of the $LnSb_2O_4Br$ series (*Ln* = Eu–Tb) with vertex-connected $[SbO_3]^{3-}$ ψ^1-tetrahedra as dominant structural feature.

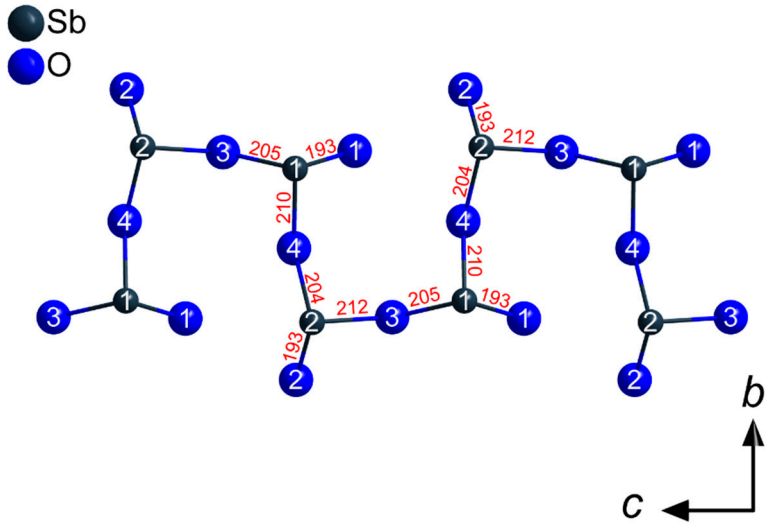

Figure 4. Network of vertex-connected $[SbO_3]^{3-}$ ψ^1-tetrahedra in the crystal structure of the $LnSb_2O_4Br$ series (*Ln* = Eu–Tb) building up meandering strands of the composition $^1_\infty\{[SbO^v_{2/2}O^t_{1/1}]^-\}$ along [001]. The given interatomic Sb–O distances (in pm) are valid for $TbSb_2O_4Br$.

In valentinite and senarmontite, the two natural crystalline modifications of Sb_2O_3, the antimony(III)-oxygen distances feature values of 198–202 pm and therefore fall in between the range of our refined distances for the $LnSb_2O_4Br$ series with regards to the differences of the linking and the terminal oxygen

atoms [46,47]. Consequently, the sharing of an oxygen atom between two antimony(III) cations leads to an expansion of the respective bond length by at least 10 pm.

The influence of the lone electron pair of a pnictogen(III) cation has recently been reported for comparable lanthanoid(III) oxopnictogenates(III), such as the lanthanoid(III) halide oxoarsenates(III) with the compositions $Ln_5Cl_3[AsO_3]_4$ and $Ln_3X_2[As_2O_5][AsO_3]$ [12,14]. While the title compounds feature one-dimensional infinite strands of corner-connected $[SbO_3]^{3-}$ units, the latter only display isolated $[AsO_3]^{3-}$ ψ^1-tetrahedra or doubles of them in vertex-condensed $[As_2O_5]^{4-}$ pyroanions. In these condensed units, the bridging oxygen atoms also show the longest distances to the arsenic(III) cations, much like in the monoclinic members of the series $LnSb_2O_4Br$, where the bond lengths to the corner-connecting oxygen atoms of the $[SbO_3]^{3-}$ groups fall into a longer interval than the short terminal ones.

Comparing the structural features of the short $LnSb_2O_4Br$ (*Ln* = Eu–Tb) series with the crystal structure of the long $Na_2Ln_3Cl_3[TeO_3]_4$ series (*Ln* = La–Nd, Sm–Lu) featuring Te^{4+} as cation isoelectronic to Sb^{3+} reveals several similarities [48–50]. The lanthanoid(III) cations also exhibit an eightfold coordination sphere exclusively by oxygen atoms building up $[LnO_8]^{13-}$ hemiprisms and thus no Ln^{3+}-X^- bonds exist. These hemiprisms build up layers of the composition $^2_\infty\{[LnO^e_{8/2}]^{5-}\}$ parallel to the (001) plane. Furhtermore, the Te^{4+} cations are coordinated by three oxygen atoms forming $[TeO_3]^{2-}$ anions in the shape of ψ^1-tetrahedra, but in this case, without any Te^{4+}–O^{2-}–Te^{4+} contacts. The halide anions X^- are only connected to the sodium cations located in between two layers of $[LnO_8]^{13-}$ hemiprisms.

The crystallographically unique bromide anions do not exhibit any bonding contacts to the Ln^{3+} cations, since the shortest $Ln^{3+}\cdots Br^-$ separations amount to 422 pm. The bromide anions are located between planes formed by edge-connected $[LnO_8]^{13-}$ polyhedra. The antimony(III) cations connected to these oxygen atoms show distances of 318–320 pm up to 366–367 pm to the neighboring bromide anions (Figure 5). Comparing these values with ternary antimony oxide bromides seems appropriate. In $Sb_4O_5Br_2$, a well-known ternary antimony(III) oxide bromide, the Sb^{3+} cations also show only short interatomic distances to the oxygen atoms with a major contribution to chemical bonding (189–251 pm), while the bromide anions are partially even more removed away from the Sb^{3+} cations with distances of 302–366 pm [51]. Almost the same holds for a second antimony(III) oxide bromide with the composition $Sb_8O_{11}Br_2$, where Sb^{3+}–O^{2-} distances of 190–257 pm and $Sb^{3+}\cdots Br^-$ distances of 314–396 pm occur [52,53]. Therefore, in both these ternary compounds and $LnSb_2O_4Br$ (*Ln* = Eu–Tb), the Sb^{3+}–Br^- bond lengths illustrate the tendency of Sb^{3+} cations to be coordinated by bromide anions with far greater interatomic distances compared to the oxygen atoms.

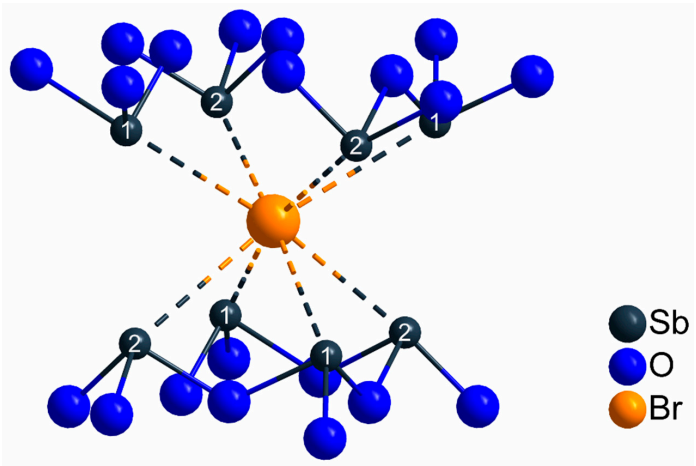

Figure 5. Coordination sphere of the crystallographically unique bromide anions in the crystal structure of the $LnSb_2O_4Br$ series (*Ln* = Eu–Tb) with shortest interatomic distances of *d*(Sb···Br) = 318–320 pm and no bonding contacts to any Ln^{3+} cation.

In Figure 6, a section of the crystal structure with indication of the cell edges, coordination polyhedra around the lanthanoid(III) cations and the refined anisotropic displacement ellipsoids is shown. The lattice parameters for all members of the LnSb$_2$O$_4$Br series (Ln = Eu–Tb) are listed in Table 1, while the crystallographic data as well as the positional atomic parameters and selected interatomic distances for EuSb$_2$O$_4$Br and TbSb$_2$O$_4$Br can be found in Tables A1–A3. In the case of GdSb$_2$O$_4$Br, it was also possible to synthesize very flat, square platelets of crystals with the desired composition, however, the quality of the obtained single crystals revealed to be too poor for a trustworthy structure refinement. Instead, it was possible to refine the unit-cell parameters of GdSb$_2$O$_4$Br both via single-crystal X-ray diffraction as well as powder X-ray diffraction methods (Section 3.2).

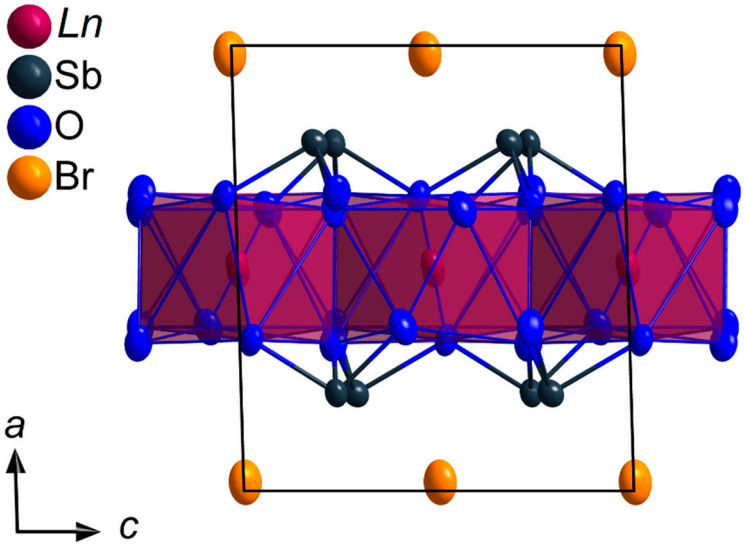

Figure 6. Section of the crystal structure of the LnSb$_2$O$_4$Br series (Ln = Eu–Tb) viewed along [010] emphasizing the unit-cell edges and $[LnO_8]^{13-}$ polyhedra (*dark red*) utilizing the refined anisotropic displacement parameters with an ellipsoidal probability of 95%.

Table 1. Lattice parameters for the three members of the LnSb$_2$O$_4$Br series (Ln = Eu–Tb) as determined by means of powder X-ray diffractometry.

Compound	EuSb$_2$O$_4$Br	GdSb$_2$O$_4$Br	TbSb$_2$O$_4$Br
Crystal system		monoclinic	
Space group		$P2_1/c$ (no. 14)	
a/pm	895.69(2)	895.67(2)	894.56(2)
b/pm	791.90(2)	789.27(2)	785.84(2)
c/pm	790.46(2)	788.44(2)	784.25(2)
β/°	91.743(1)	91.681(1)	91.625(1)

3.2. Powder X-ray Diffraction

For phase analyses of the obtained and water-washed product mixtures of all three systems, PXRD measurements were performed. Figure A2 shows the diffractogram of EuSb$_2$O$_4$Br and TbSb$_2$O$_4$Br, respectively. While good accordance among the positions of the simulated and measured reflections is observed, a remarkable variance of the relative reflection intensities occurs. This kind of texture effects can be attributed to the extreme platelet habit of the crystals (Figure 8). Intensive crushing of the powder samples and subsequent diffraction experiments showed an improvement of the relative intensities towards the theoretical values, however, strong reflex broadening was observed. Therefore, the samples were only slightly crushed to avoid these broadenings.

Since it was not possible to yield single crystals of $GdSb_2O_4Br$ with sufficient quality for a reliable structure determination, the lattice parameters were refined from powder X-ray diffraction methods. For comparison, single crystals of $GdSb_2O_4Br$ with unit-cell parameters of a = 895.54(6) pm, b = 788.91(5) pm, c = 787.67(5) pm and β = 91.725(3)° were observed. The experimental and simulated pattern as well as the plot of the calculated deviation and the Bragg positions are given in Figure 7. The refined cell parameters for $GdSb_2O_4Br$ are also given in Table 1 and are in high accordance with the values deriving from the single-crystal measurement as well as with the expected ones due to the lanthanoid contraction.

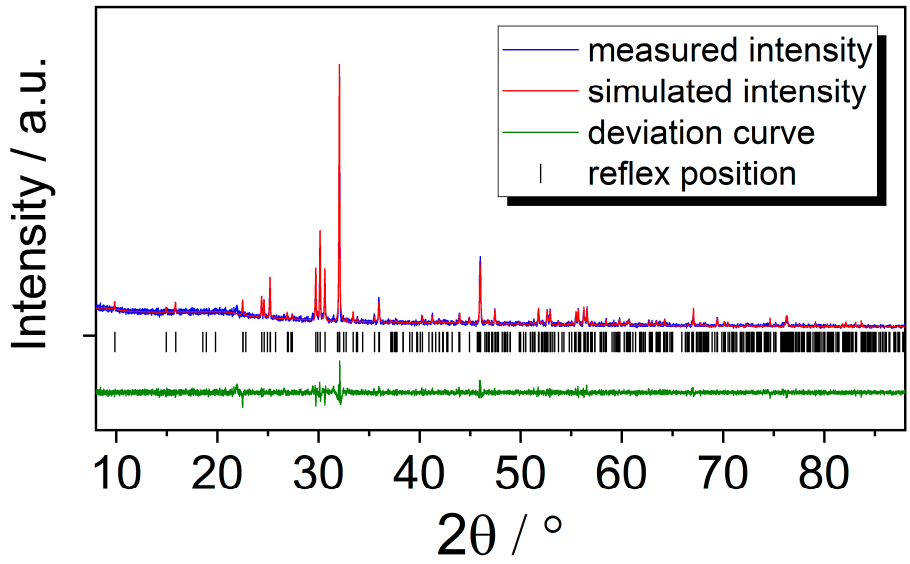

Figure 7. Le Bail profile matching of $GdSb_2O_4Br$ showing the measured pattern (blue), the simulated pattern (red), the deviation plot (green), and the reflex positions (black).

3.3. Electron-Probe Microanalysis

To evaluate the crystal morphology of the three $LnSb_2O_4Br$ representatives with Ln = Eu–Tb, scanning electron images were recorded. In Figure 8, representative micrographs of all three compounds illustrating the size and crystal habit of the synthesized crystals are given. A prominent feature for all three compounds is the formation of platelet-shaped crystals.

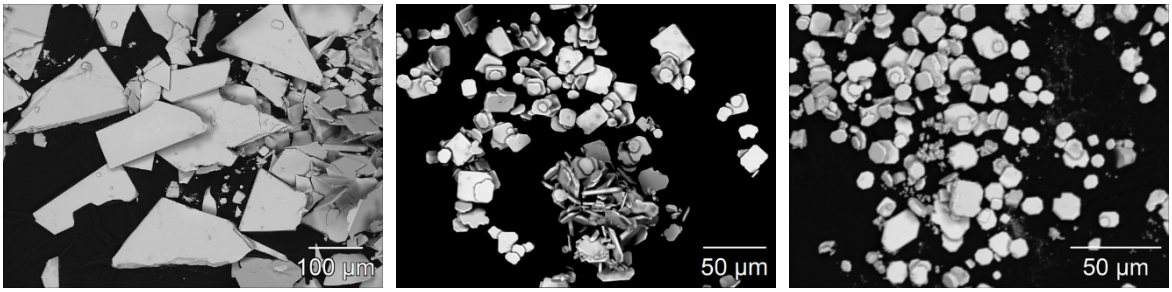

(**a**) (**b**) (**c**)

Figure 8. Scanning electron images of $EuSb_2O_4Br$ (**a**), $GdSb_2O_4Br$ (**b**), and $TbSb_2O_4Br$ (**c**) illustrating the platelet crystal habit with typical edge lengths of 50–150 µm for the europium compound and 10–35 µm for the gadolinium and terbium representatives.

All members of the $LnSb_2O_4Br$ series (Ln = Eu–Tb) were characterized with energy-dispersive X-ray spectroscopy to verify the purity and validate the absence of unintended elements in the gained crystals. As shown in Figure 9, each compound exhibits the emission lines of the intended elements and no additional ones are present in the examined samples.

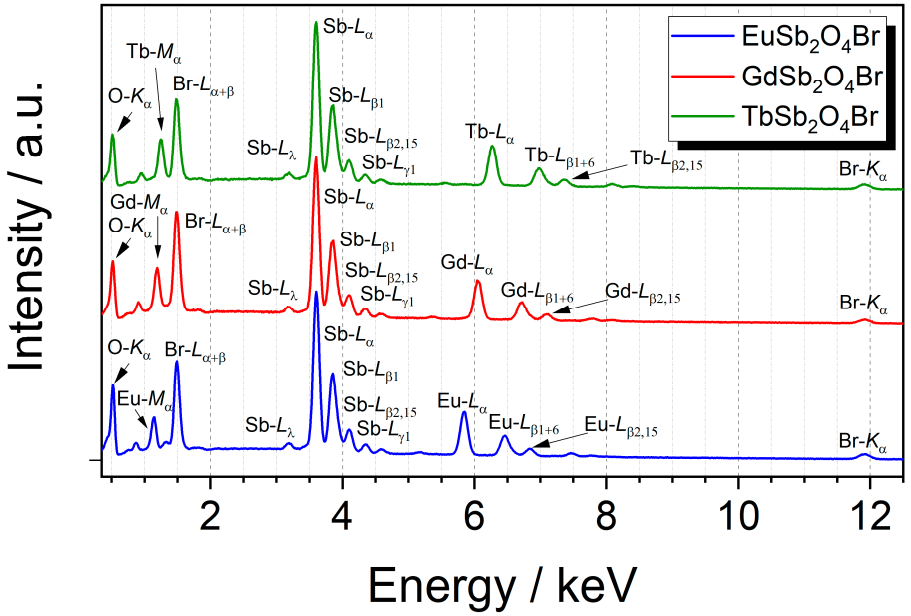

Figure 9. Energy-dispersive X-ray spectra of the LnSb$_2$O$_4$Br series with Ln = Eu–Gd at an acceleration voltage of 20 kV with assignment of the relevant emission lines.

For an europium(III)-doped sample of TbSb$_2$O$_4$Br as representative of the series, quantitative measurements of the single crystals were performed. This was of special interest, since previous structure studies about the crystal structures in the quaternary system Sm–Sb–O–X (X = Cl and Br) revealed a mixed-Ln^{3+}/Sb^{3+} occupancy of the Sb^{3+} position and, therefore, an incoherency with the theoretical formula "SmSb$_2$O$_4X$" [26]. For this new structure type in the quaternary system Ln-Sb-O-Br with similarities regarding structural features and synthesis methods, it seemed appropriate to apply a second method to confirm the determined composition of at least one representative with the formula LnSb$_2$O$_4$Br (Ln = Eu–Tb). Moreover, the method was applied to determine the degree of doping in TbSb$_2$O$_4$Br, since it is not possible to refine the europium(III) content in a terbium(III) host lattice by means of X-ray diffraction methods.

The results of the quantitation using wavelength-dispersive spectrometry are compiled in Table A4. When comparing the experimental values to the expected of TbSb$_2$O$_4$Br doped with 1.5 at-% Eu^{3+} regarding the total amount of lanthanoid(III) cations, the measurements validate formula TbSb$_2$O$_4$Br:Eu^{3+} with the desired doping content.

3.4. Photoluminescence Spectroscopy

Antimony(III) compounds are known to show an excitation band in the ultraviolet range (UV) with a maximum around 270 nm corresponding to the partially forbidden $^1S_0 \rightarrow {}^3P_1$ electronic transition. The Sb^{3+} emission $^3P_1 \rightarrow {}^1S_0$ is known to occur over a broad range (from 300 to 650 nm), and often overlaps the excitation range of trivalent lanthanoid cations, such as Eu^{3+} and Tb^{3+}, rendering it potentially a suitable sensitizer for lanthanoid emission [54,55]. The luminescence of Sb^{3+} in LnSb$_2$O$_4$Br representatives with Ln = Eu–Tb can be best investigated in GdSb$_2$O$_4$Br as Gd^{3+} only emits in the UV (typically around 310 nm) due to a transition from the $^6P_{7/2}$ to $^8S_{7/2}$ levels. However, even efficient sensitization of Gd^{3+} has been reported in YPO$_4$:Sb^{3+}, Gd^{3+} [7]. The excitation spectrum of GdSb$_2$O$_4$Br monitored at 455 nm shows a band with a maximum at 257 nm, which can be assigned to the the partially forbidden $^1S_0 \rightarrow {}^3P_1$ electronic transition of Sb^{3+} (Figure 10).

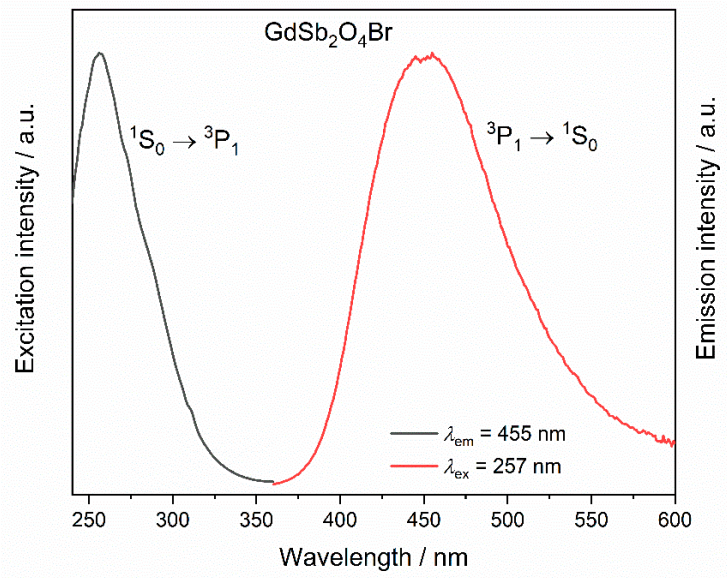

Figure 10. Excitation (λ_{em} = 455 nm) and emission spectra (λ_{ex} = 257 nm) of $GdSb_2O_4Br$.

Upon excitation into 257 nm, a broad band is visible in the emission spectrum in the region between 400 and 500 nm (Figure 10), with a maximum at 455 nm, corresponding to the transition $^3P_1 \rightarrow {}^1S_0$. This band in the blue region of the electromagnetic spectrum occurs for all the investigated compounds upon excitation in $^1S_0 \rightarrow {}^3P_1$ (inset in Figure 11, left). For $TbSb_2O_4Br:Eu^{3+}$ and $GdSb_2O_4Br:Eu^{3+}$ its intensity is negligible compared to the Eu^{3+} transitions (Figure 11, left) and less intense than Tb^{3+} transitions in the terbium derivatives (inset in Figure 11, left), suggesting the presence of an energy transfer (ET) from Sb^{3+} to Ln^{3+}. The different contribution of the Sb^{3+} emission (blue region) compared to the Eu^{3+} emission (red region) as well as Tb^{3+} role, are demonstrated by the chromaticity coordinates calculated for $TbSb_2O_4Br:Eu^{3+}$ and $GdSb_2O_4Br:Eu^{3+}$ (λ_{ex} = 257 nm) (Figure 11, *right*). In order to explain this difference, a deep investigation on the luminescence properties of both $TbSb_2O_4Br:Eu^{3+}$ and $GdSb_2O_4Br:Eu^{3+}$ was performed.

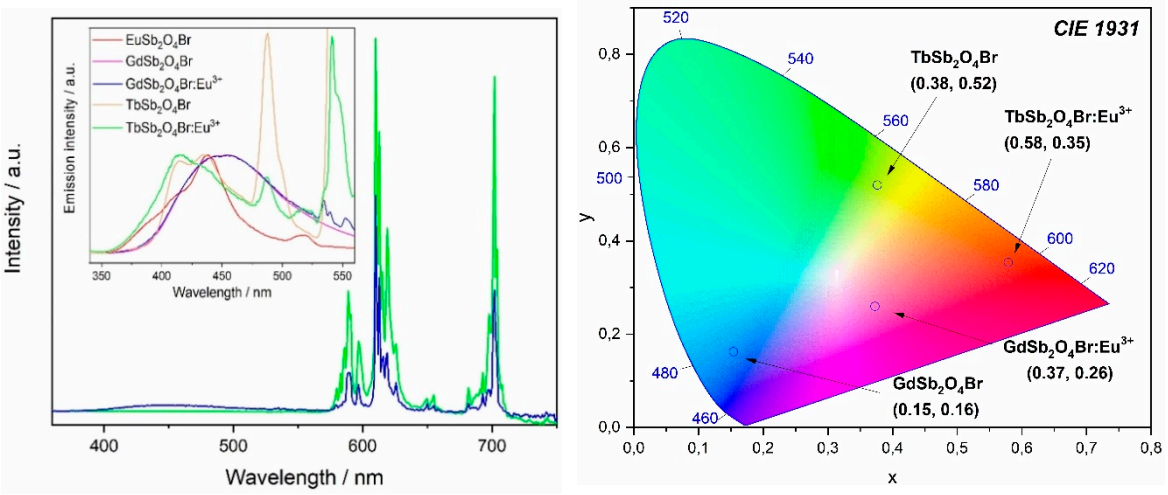

Figure 11. Left: emission spectra of $TbSb_2O_4Br:Eu^{3+}$ (green line) and $GdSb_2O_4Br:Eu^{3+}$ (blue line) at λ_{ex} = 257 nm. Inset: comparison of emission in the Sb^{3+} region for all the compounds upon the same excitation. These spectra were normalized for the respective Sb^{3+} emission maximum of each compound. **Right**: Commission internationale de l'éclairage (CIE) diagram (CIE 1931) for $TbSb_2O_4Br$, $TbSb_2O_4Br:Eu^{3+}$, $GdSb_2O_4Br$, and $GdSb_2O_4Br:Eu^{3+}$ at λ_{ex} = 257 nm.

Excitation spectra of $EuSb_2O_4Br$, $GdSb_2O_4Br:Eu^{3+}$, and $TbSb_2O_4Br:Eu^{3+}$ are shown in Figure 12. For $EuSb_2O_4Br$, when monitoring at 611 nm, the most intense band appears at 464 nm, which belongs to the set of $^7F_0 \rightarrow {}^5D_2$ hypersensitive dielectric dipole transitions of Eu^{3+}. The other excitation lines correspond to $^7F_0 \rightarrow {}^5L_6$ at 393 nm, $^7F_0 \rightarrow {}^5D_1$ and $^7F_1 \rightarrow {}^5D_1$ at 525 and 534 nm of Eu^{3+}, respectively.

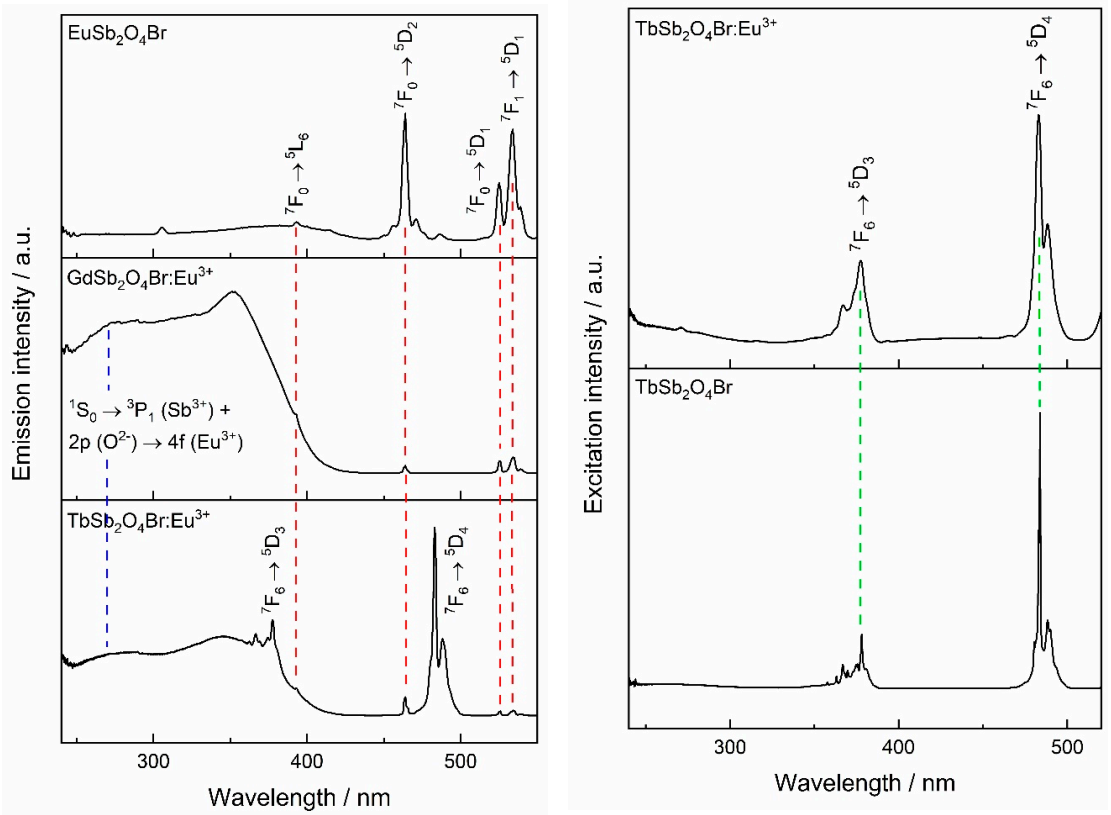

Figure 12. Left: excitation spectra of Eu^{3+}-containing $LnSb_2O_4Br$ compounds (Ln = Eu–Tb), monitored at λ_{em} = 611 nm. **Right**: excitation spectra of Tb^{3+}-based compound $TbSb_2O_4Br$, monitored at λ_{em} = 541 nm.

All the aforementioned transitions can also be observed in the two Eu^{3+}-doped compounds, $GdSb_2O_4Br:Eu^{3+}$ and $TbSb_2O_4Br:Eu^{3+}$. Moreover, in both the Eu^{3+}-doped compounds, two broad bands can be detected in the UV region. In addition to the band around 250 nm, a second broad band at higher wavelength can be observed, which is attributed to the $2p$ (O^{2-}) → $4f$ (Eu^{3+}) charge transfer which frequently is observed in Eu^{3+} oxide compounds [6,56–58]. Due to the eight-fold coordination of the lanthanide cations in $GdSb_2O_4Br:Eu^{3+}$ and $TbSb_2O_4Br:Eu^{3+}$ and to their similar radii, both compounds are supposed to have charge transfer bands in the region around 260–270 nm, similarly to $Gd_2Zr_2O_7:Eu^{3+}$ and $LaPO_4:Eu^{3+}$ [57]. Thus in the ultraviolet (UV) region, an overlap between the aforementioned $^1S_0 \rightarrow {}^3P_1$ transition of Sb^{3+} and the Eu^{3+} charge transfer band occurs. For $GdSb_2O_4Br:Eu^{3+}$, the charge transfer band is the most intense. Conversely, it is negligible in the neat Eu-compound.

By monitoring the Eu^{3+} emission at 611 nm in $TbSb_2O_4Br:Eu^{3+}$, besides the characteristic interconfigurational f–f transitions of Eu^{3+}, albeit with comparatively weak relative intensity, the bands in the UV region of light belonging to Eu^{3+}–O^{2-} charge transfer and the Sb^{3+} $^1S_0 \rightarrow {}^3P_1$ transitions can be seen. In addition, transitions characteristic for Tb^{3+} are present which points to $Tb^{3+} \rightarrow Eu^{3+}$ sensitization.

Excitation spectra monitored at the Tb^{3+} emission for $TbSb_2O_4Br$ as well as $TbSb_2O_4Br:Eu^{3+}$ are shown in Figure 12 (right). Both materials show the characteristic bands of Tb^{3+} which can be assigned to the $^7F_6 \rightarrow {}^5D_3$ and $^7F_6 \rightarrow {}^5D_4$ transitions. The presence of Tb^{3+} peaks in the excitation spectrum

of $TbSb_2O_4Br:Eu^{3+}$ when detecting the Eu^{3+} emission indicates the presence of the $Tb^{3+} \rightarrow Eu^{3+}$ energy transfer.

When excited at 283 and 464 nm,, corresponding to $^1S_0 \rightarrow {}^3P_1$ of Sb^{3+}, charge transfer band, $^7F_0 \rightarrow {}^5L_6$ and $^7F_0 \rightarrow {}^5D_2$ of Eu^{3+}, respectively (Figure 13), all Eu^{3+}-containing compounds show emission from the $^5D_0$ level of Eu^{3+} transitions. The low site symmetry of Eu^{3+} in the compound series increases the number of observable transitions [6]. The hypersensitive (or electric dipole) band $^5D_0 \rightarrow {}^7F_2$ with five sublevels, and the magnetic dipole transition $^5D_0 \rightarrow {}^7F_1$ with all three possible sublevels can be observed.

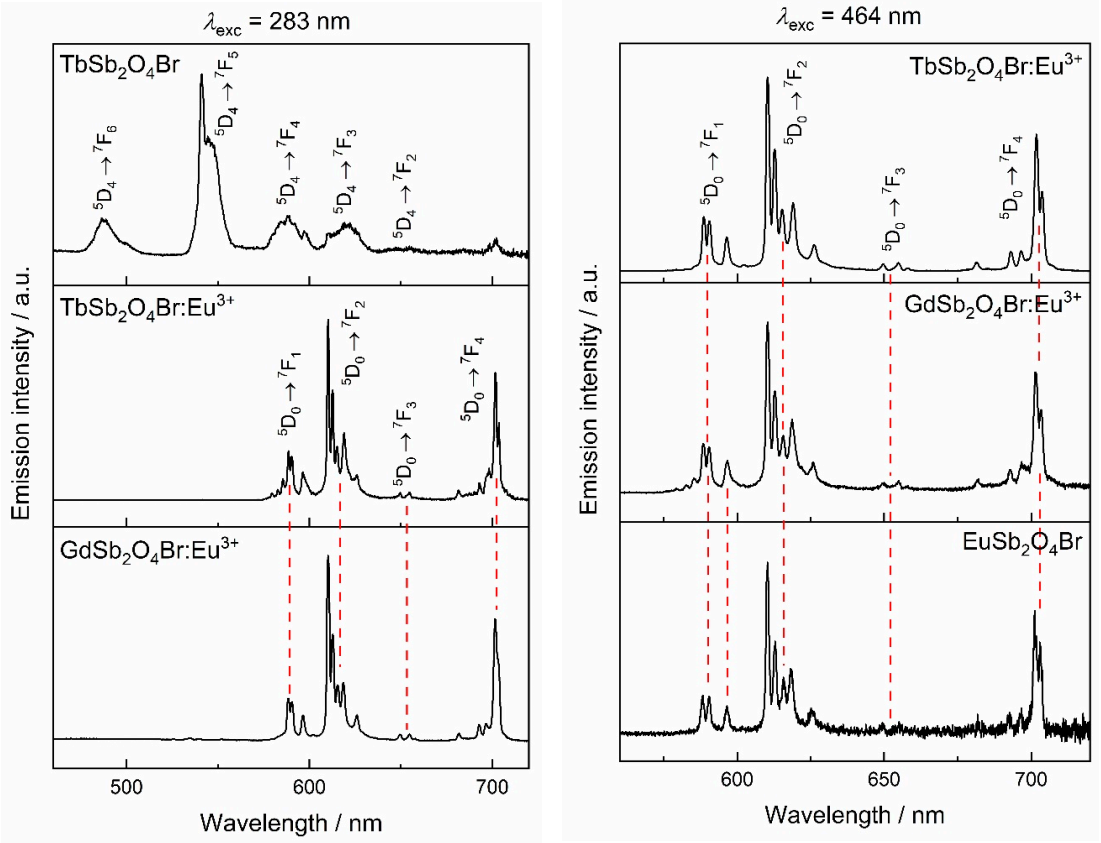

Figure 13. Left: emission spectra upon excitation at the charge-transfer band of the Ln^{3+} matrix (λ_{ex} = 283 nm). **Right**: emission spectra excited in the characteristic Eu^{3+} $^7F_0 \rightarrow {}^5D_2$ transiton (λ_{ex} = 464 nm).

The dominance of the $^5D_0 \rightarrow {}^7F_2$ transition in the emission spectra relative to the $^5D_0 \rightarrow {}^7F_1$ transition is compatible with the location of Eu^{3+} in a low-symmetry site [59]. The asymmetry ratio, defined as $(^5D_0 \rightarrow {}^7F_2)/(^5D_0 \rightarrow {}^7F_1)$, is a parameter that indicates the distortion of Eu^{3+} site with respect to an inversion centre. As expected, the asymmetry ratio is significantly larger than 1 indicating a low-symmetry site, in agreement with a site symmetry of 1 for Ln^{3+} in $LnSb_2O_4Br$ [59,60].

Very weak peaks corresponding to emission from higher levels are also visible: at 582 nm, attributable to the forbidden transition $^5D_1 \rightarrow {}^7F_0$ and at 579 nm, that probably corresponds to the $^5D_1 \rightarrow {}^7F_3$ transition and others even weaker in the 560–576 nm region [5]. The intensity of the $^5D_0 \rightarrow {}^7F_4$ transition is higher than the magnetic dipole band, as already found in lanthanoid(III) orthoborates with C_s sites symmetry [61] or in the polyoxometalate $Na_9[EuW_{10}O_{36}] \cdot 14\ H_2O$ with a distorted D_{4d} symmetry [62].

Due to the full Eu^{3+} concentration, a partial quenching of Eu^{3+} emission occurs in $EuSb_2O_4Br$. This is confirmed not only by the short lifetime of $^5D_0 \rightarrow {}^7F_2$ detected upon excitation at 464 nm (10.7 μs), but also by the absence of the transitions from levels higher than $^5D_0$. As can be observed

in the excitation spectrum (Figure 12, left) by detecting the most intense Eu^{3+} emission at 611 nm, no excitation transitions are present in the UV region, and for this reason, the sample does not show any emission upon excitation at 257 nm and was not included in the CIE (Commission internationale de l'éclairage) diagram. Nevertheless, upon excitation in the most intense excitation transition at 464 nm, corresponding to the $^7F_0 \rightarrow {}^5D_2$ transition of Eu^{3+}, $EuSb_2O_4Br$ shows the characteristic luminescence features of Eu^{3+}. This means that energy migration between ions in the bulk is not completely efficient upon excitation at lower energy.

The emission spectrum of the Tb^{3+}-based materials upon excitation with $\lambda_{ex} = 378$ nm are shown in Figure 14. The spectrum of $TbSb_2O_4Br$ shows $^5D_4 \rightarrow {}^7F_6$, $^5D_4 \rightarrow {}^7F_5$, $^5D_4 \rightarrow {}^7F_4$, $^5D_4 \rightarrow {}^7F_3$ transitions, resulting overall in an impression of green light. In the Eu^{3+}-doped compound, $TbSb_2O_4Br:Eu^{3+}$, emission from Eu^{3+} are dominant whilst those for Tb^{3+} are hardly visible. Together with the presence of Tb^{3+} excitation bands by monitoring the luminescence of Eu^{3+}, the strong Eu^{3+} emission at the expense of Tb^{3+} emission, indicates the presence of notable $Tb^{3+} \rightarrow Eu^{3+}$ energy transfer. Moreover, this can explain the red shift in the CIE diagram with respect to $GdSb_2O_4Br:Eu^{3+}$: in $TbSb_2O_4Br:Eu^{3+}$, $Sb^{3+} \rightarrow Eu^{3+}$ is mediated by Tb^{3+}, that in turn transfers almost all the excitation light to Eu^{3+}, shifting the final emission towards the red, while in $GdSb_2O_4Br:Eu^{3+}$ some Sb^{3+} contribution is still present, giving a combination of both red and blue contributions.

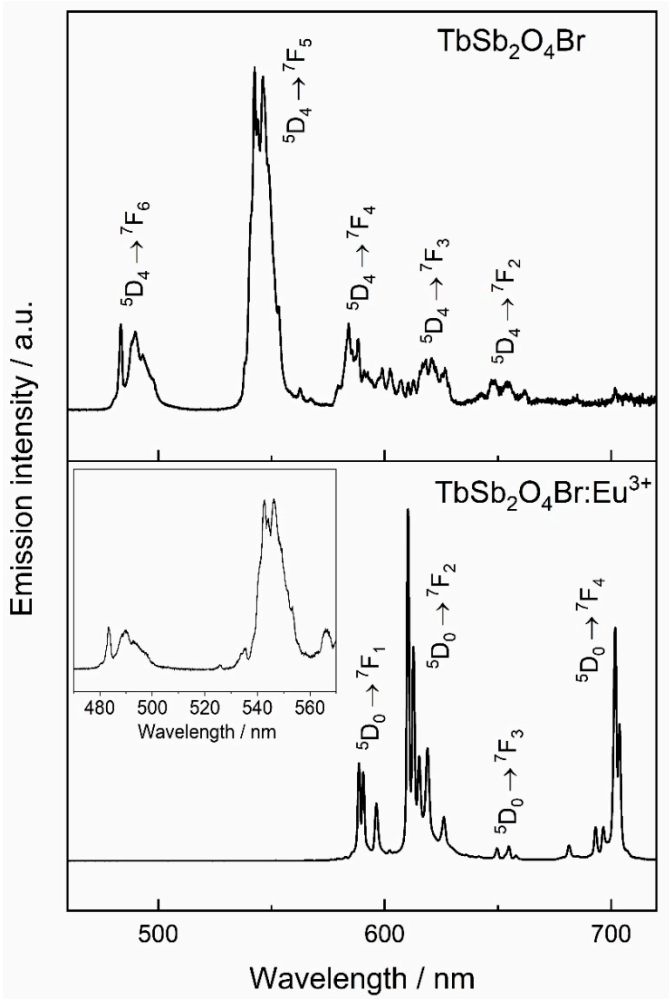

Figure 14. Tb^{3+}-based materials upon excitation at 378 nm, corresponding to the $^7F_6 \rightarrow {}^5D_3$ transition of Tb^{3+}. The inset in the bottom part of the figure shows a magnification of Tb^{3+} emission in the Eu^{3+}-doped compound $TbSb_2O_4Br$ emphasizing the less intense Tb^{3+} transitions.

Analysis of the luminescence decays were performed in order to better investigate the interactions (i.e., radiative and non-radiative processes) involved between the emitting cations, such as energy transfer (ET) and concentration quenching.

The Eu^{3+} emission (611 nm), upon excitation with λ_{ex} = 257 nm (corresponding to the $^1S_0 \rightarrow {}^3P_1$ electronic transition of Sb^{3+}) was probed in order to allow for a comparison of the optical properties of $GdSb_2O_4Br:Eu^{3+}$ and $TbSb_2O_4Br:Eu^{3+}$ (see also the CIE diagram, Figure 11, *right*).

Upon this excitation, an intensity rise time can be seen for both the decay curves of $GdSb_2O_4Br:Eu^{3+}$ and $TbSb_2O_4Br:Eu^{3+}$, indicating that Eu^{3+}-emitting levels are fed by energy transfer processes. The corresponding lifetime values were calculated as a weighted average of the two components [63]. As previously discussed, a difference between excitation spectra of the two materials is noticeable when monitoring the Eu^{3+} emission at 611 nm: In $TbSb_2O_4Br:Eu^{3+}$ the main peak occurs at 488 nm, followed by the peak at 378 nm, both belonging to Tb^{3+}, while the bands in the UV region have a minor importance. This demonstrates the major role of Tb^{3+} in sensitizing the emission of Eu^{3+}, allowing a color more shifted towards the red. By contrast, in $GdSb_2O_4Br:Eu^{3+}$, Eu^{3+} emission can only be sensitized through Sb^{3+} energy transfer. This is related to the greater role played by the blue component in the final emission, as shown in the different color coordinates in the CIE diagram. (see Figure 11, right).

Moreover, the lifetimes of both doped materials, $TbSb_2O_4Br:Eu^{3+}$ and $GdSb_2O_4Br:Eu^{3+}$, are dependent on the excitation wavelength, as an example, a comparison between the decays of $GdSb_2O_4Br:Eu^{3+}$ upon excitation in the $^1S_0 \rightarrow {}^3P_1$ electronic transition of Sb^{3+} at 257 nm vs. excitation in the Eu^{3+} transition at $^7F_0 \rightarrow {}^5L_6$ at 393 nm is shown in Figure 15 (right).

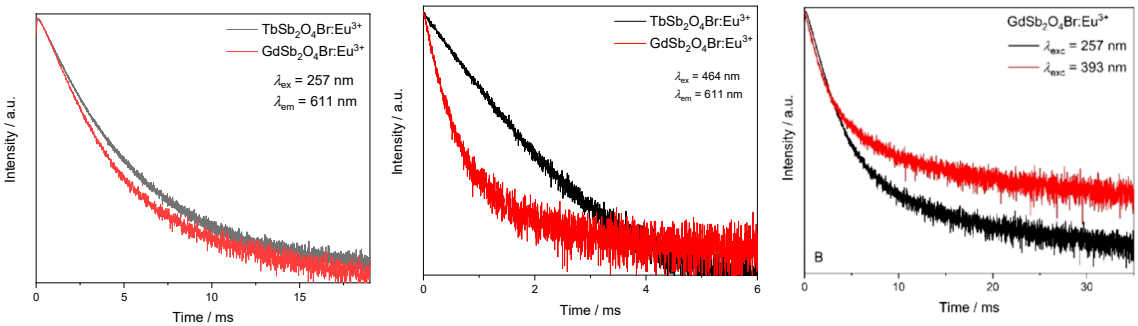

Figure 15. Lifetime comparison upon excitation at 257 nm between the Eu^{3+} emission monitored at λ_{em} = 611 nm in the different matrices ($GdSb_2O_4Br$ and $TbSb_2O_4Br$, **left**); upon excitation at 464 nm (**middle**); and for $GdSb_2O_4Br:Eu^{3+}$ upon excitation at λ_{ex} = 257 nm and λ_{ex} = 393 nm (**right**). All the intensity decays are reported on a logarithm (log) intensity scale.

Eu^{3+} lifetime corresponding to the main emission at 611 nm was also evaluated upon excitation in the most intense band at 464 nm ($^7F_0 \rightarrow {}^5D_2$ of Eu^{3+}). In $TbSb_2O_4Br:Eu^{3+}$, a single exponential intensity decay was observed and an excited state lifetime of about 0.8 ms could be calculated. The single exponential behavior reflects the occupation of only one crystallographic site by Eu^{3+}. The observed lifetime is similar to the value observed for Eu^{3+} in zirconia samples [56], as well as with antimony–germanate–silicate glasses [63]. However, for excitation of $GdSb_2O_4Br:Eu^{3+}$ with 464 nm, the decay curve needed to be fitted bi-exponential (Figure 15, middle and fitted components in Table A5), pointing to two different Eu^{3+} emitting species, either with different environment, potentially Eu^{3+} in the bulk and Eu^{3+} as the surface (note that it was not possible to obtain single crystals of $GdSb_2O_4Br$ of sufficient quality for single crystal X-ray diffraction (SCXRD) analysis).

The efficiency of $Tb^{3+} \rightarrow Eu^{3+}$ was evaluated through lifetime analysis, by using the formula:

$$\eta_{ET} = 1 - \tau_{DA}\ \tau_D{}^{-1} \quad (2)$$

where τ_{DA} is the lifetime of the donor (Tb^{3+}) in presence of the acceptor (Eu^{3+}), and τ_D is the lifetime of the donor in the undoped material.

Thus, the emission decays corresponding to the Tb^{3+} emission from the $^5D_4$ level were acquired by exciting into the most intense excitation band, namely 483 nm (corresponding to the $^7F_6 \rightarrow {}^5D_4$ transition), for both $TbSb_2O_4Br$ and $TbSb_2O_4Br:Eu^{3+}$ (Figure 16). The undoped sample shows a double exponential decay. The total lifetime of 0.25 ms can be calculated as a weighted average of the two components as reported by Zmojda et al. [63], while the Eu^{3+}-doped sample shows a value of 12.3 µs, fitted by a single exponential decay. The η_{ET} obtained from these values is around 95%.

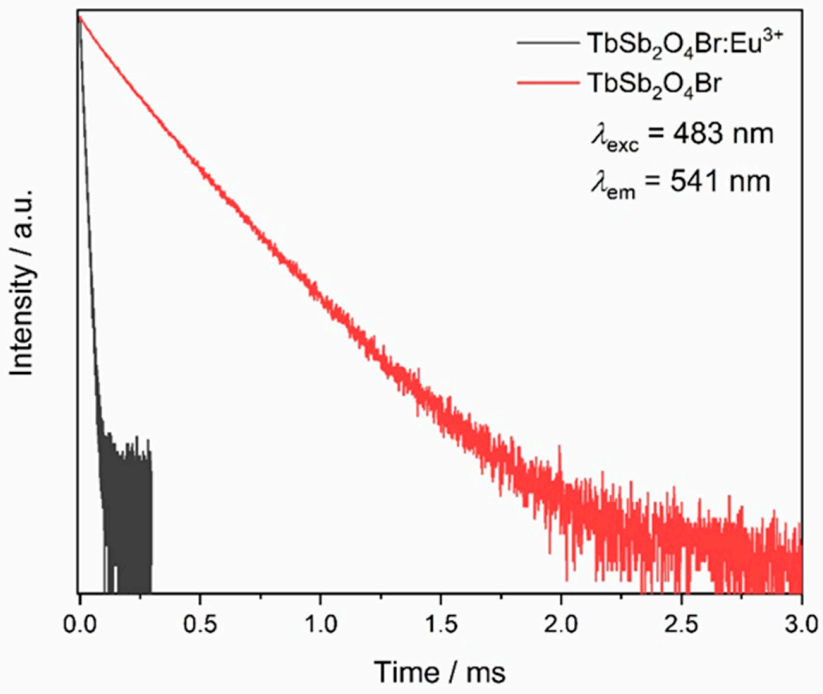

Figure 16. Lifetimes of terbium based compounds. The Tb^{3+} emission at λ_{em} = 541 nm is monitored upon excitation at λ_{exc} = 483 nm for both the Eu^{3+}-doped and the undoped $TbSb_2O_4Br$ samples.

4. Conclusions

LnSb_2O_4Br series (*Ln* = Eu–Tb) presents a new material class of quaternary lanthanoid(III) oxoantimonate(III) halides. With respect to the hitherto reported quaternary samarium(III) oxoantimonate(III) halides, the presented compounds show structural similarities, such as the eightfold oxygen-coordination sphere of the lanthanoid(III) cations, but no mixed-occupied sites for the Ln^{3+} and Sb^{3+} cations. Besides $La_5F_3[SbO_3]_4$, the reported compounds can be viewed as a new composition type in the quaternary systems *Ln*(III)–Sb(III)–O–*X* without mixed-occupation sites so far. As important structural features, the lanthanoid(III) cations are coordinated exclusively by eight oxygen atoms in the shape of $[LnO_8]^{13-}$ hemiprisms. As second structural feature worth mentioning, the antimony(III) cations build up meandering strands of vertex-connected $[SbO_3]^{3-}$ anions and, therefore, show a remarkable difference to the already reported lanthanoid(III) halide oxopnictogenates(III) such as $La_5F_3[SbO_3]_4$ or $Ln_3X_2[As_2O_5][AsO_3]$, where mostly isolated or vertex-shared $[PnO_3]^{3-}$ anions as dimers are present.

Whilst the bulk europium compound, $EuSb_2O_4Br$, is not suitable as luminescent material, both $GdSb_2O_4Br$ and $TbSb_2O_4Br$ doped with Eu^{3+} show strong photoluminescence thanks to Sb^{3+} which is acting as a blue-emitting species and sensitizer for lanthanide. $TbSb_2O_4Br$:Eu additionally benefits form strong energy transfer from Tb^{3+} to Eu^{3+}. Since Sb^{3+} is emitting in the blue, Tb^{3+} in the green and Eu^{3+} in the red white-light emitting materials can be envisioned in this class of compound.

Author Contributions: F.C.G. synthesized the title compounds $LnSb_2O_4Br$ (*Ln* = Eu–Tb). F.C.G. and T.S. solved their crystal structures. Funds provided to T.S. funded the chemicals, the materials, the scientific equipment and the infrastructure for synthesis, single-crystal and powder X-ray diffraction measurements as well as electron-probe microanalysis. F.C.G. investigated the $LnSb_2O_4Br$ series (*Ln* = Eu–Tb) via electron-beam X-ray microprobe techniques. V.P. performed the photoluminescence measurements with the scientific equipment provided by support to A.-V.M., V.P. and K.V.D. were supported by fellowships provided by the Göran Gustafsson prize in Chemistry, Royal Swedish Academy of Sciences, to A.-V.M., V.P. and A.-V.M. interpreted the the data. F.C.G., V.P., K.V.D. and A.-V.M. wrote the initial paper, A.-V.M. and T.S. reviewed it carefully. All authors have read and agreed to the published version of the manuscript.

Funding: This research was funded by the State of Baden-Württemberg (Stuttgart).

Acknowledgments: The authors would like to thank Falk Lissner for the single-crystal X-ray diffraction measurements. A.-V.M. acknowledges the Royal Swedish Academy of Sciences for support through the Göran Gustafsson prize in Chemistry and Stockholm University.

Conflicts of Interest: The authors declare no conflict of interest.

Appendix A

Table A1. Crystallographic data of the end-members of the $LnSb_2O_4Br$ series (*Ln* = Eu and Tb).

Formula	$EuSb_2O_4Br$	$TbSb_2O_4Br$
Crystal system	monoclinic	
Space group	$P2_1/c$ (no. 14)	
Lattice constants, a/pm	895.69(6)	895.37(6)
b/pm	791.82(5)	786.14(5)
c/pm	790.38(5)	785.09(5)
β/°	91.817(3)	91.638(3)
Formula units, Z	4	
Calculated density, D_x/g·cm^{-3}	6.394	6.569
Molar volume, V_m/cm^3·mol^{-1}	84, 36	83, 17
Diffractometer	StadiVari (STOE, four-circle diffractometer)	
Wavelength (λ/pm)	71.07 (Mo-K_α)	
$F(000)$	928	936
$2\theta_{max}$/°	63.58	63.72
hkl range ($\pm h_{max}$, $\pm k_{max}$, $\pm l_{max}$)	13, 11, 11	12, 11, 11
Observed reflections	19853	12173
Unique reflections	1840	1438
Absorption coefficient, μ/mm^{-1}	27.68	29.52
Absorption correction	numerical (Stoe X-Shape 2.21)	
R_{int}/R_σ	0.076/0.041	0.078/0.045
R_1/R_1 with $\|F_O\| \geq 4\sigma(F_O)$	0.055/0.034	0.047/0.033
wR_2/GooF	0.082/1.047	0.071/1.019
Structure determination and refinement	Program package ShelX-1997 [31,32]	
Extinction coefficient, ε/pm^{-3}	0.00012(9)	0.00022(9)
Residual electron density, ρ/e$^-$ 10^{-6} pm^{-3}	+1.91/−1.78	+2.02/−1.95
CCDC number	CSD-2016635	CSD-2016636

Table A2. Fractional atomic coordinates and coefficients of the equivalent isotropic displacement parameters of $EuSb_2O_4Br$ (top) and $TbSb_2O_4Br$ (bottom). All atoms occupy the general Wyckoff site 4*e*.

Atom	*x*/*a*	*y*/*b*	*z*/*c*	U_{eq}/pm^2
Eu	0.48857(4)	0.23760(5)	0.50274(5)	104(1)
Sb1	0.78149(6)	0.05812(7)	0.75756(7)	108(1)
Sb2	0.21659(6)	0.00677(7)	0.79543(7)	103(1)
O1	0.6332(6)	0.0021(7)	0.5856(7)	147(12)
O2	0.3642(6)	0.1758(7)	0.7481(7)	123(11)
O3	0.6656(6)	0.0086(7)	0.9703(7)	112(11)
O4	0.6686(6)	0.2105(7)	0.2594(7)	107(10)
Br	0.02117(11)	0.23521(12)	0.50388(12)	205(2)
Tb	0.48990(4)	0.23728(5)	0.50185(5)	85(1)
Sb1	0.78039(6)	0.05548(7)	0.75626(7)	92(2)
Sb2	0.21888(6)	0.00810(7)	0.79380(7)	90(1)
O1	0.6321(6)	0.0028(7)	0.5804(7)	128(14)
O2	0.3675(6)	0.1777(7)	0.7465(7)	111(13)
O3	0.6617(6)	0.0069(7)	0.9696(7)	100(13)
O4	0.6686(6)	0.2102(7)	0.2597(7)	118(13)
Br	0.01915(12)	0.23617(11)	0.50403(11)	188(2)

Table A3. Selected interatomic distances (*d*/pm, e.s.d.: ±0.5 pm) for $EuSb_2O_4Br$ (left) and $TbSb_2O_4Br$ (right).

Contact	$EuSb_2O_4Br$	$TbSb_2O_4Br$
Ln–O1	228.7	226.6
Ln–O1′	235.2	231.4
Ln–O2	231.9	228.7
Ln–O2′	237.1	235.4
Ln–O3	256.4	253.0
Ln–O3′	257.7	254.9
Ln–O4	255.8	252.9
Ln–O4′	258.4	257.7
Sb1–O1	192.2	193.3
Sb1–O3	204.5	204.5
Sb1–O4	209.3	209.7
Sb2–O2	192.6	192.7
Sb2–O3	210.3	212.0
Sb2–O4	205.7	204.0
Br–Sb1	328.8	327.9
Br–Sb1′	329.7	328.6
Br–Sb1″	360.6	358.7
Br–Sb1‴	360.8	358.8
Br–Sb2	318.4	318.3
Br–Sb2′	337.5	337.0
Br–Sb2″	344.8	343.9
Br–Sb2‴	367.2	366.2

Table A4. Quantitative electron-beam microprobe analysis of $TbSb_2O_4Br$ doped with 1.5 at-% Eu^{3+} using wavelength-dispersive spectrometry and the Pouchou and Pichoir (PaP) matrix correction algorithm. The oxygen content was calculated stoichiometrically.

Ion	Emission Line	Content (wt-%)	Normalized Content (at-%)	Theoretical Content (at-%)
Tb^{3+}	L_α	28.0(8)	12.3(3)	12.31
Eu^{3+}	L_α	0.43(7)	0.20(3)	0.19
Sb^{3+}	L_α	43.2(7)	25.0(4)	25.00
Br^-	K_α	14.4(7)	12.6(6)	12.50
O^{2-}	–	11.6(9)	49.9(9)	50.00

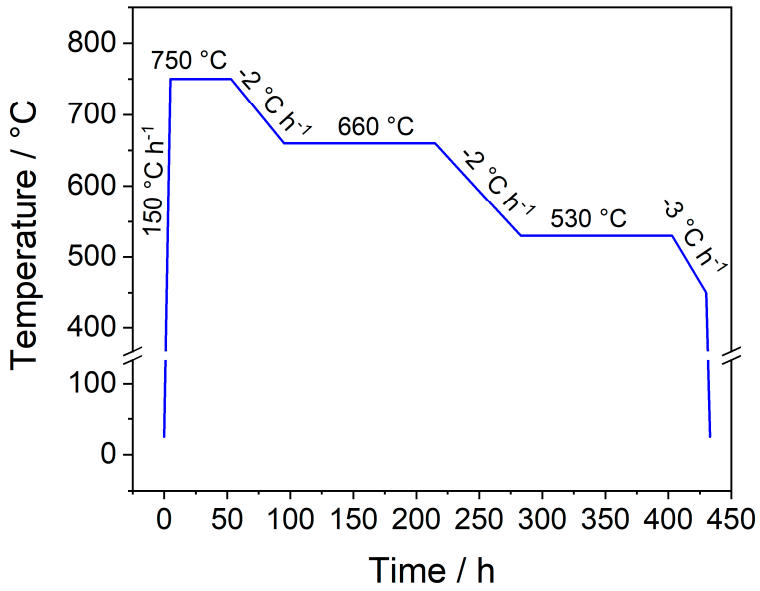

Figure A1. Applied multi-stage furnace program for the synthesis of single crystals with the composition $LnSb_2O_4Br$ (*Ln* = Eu–Tb).

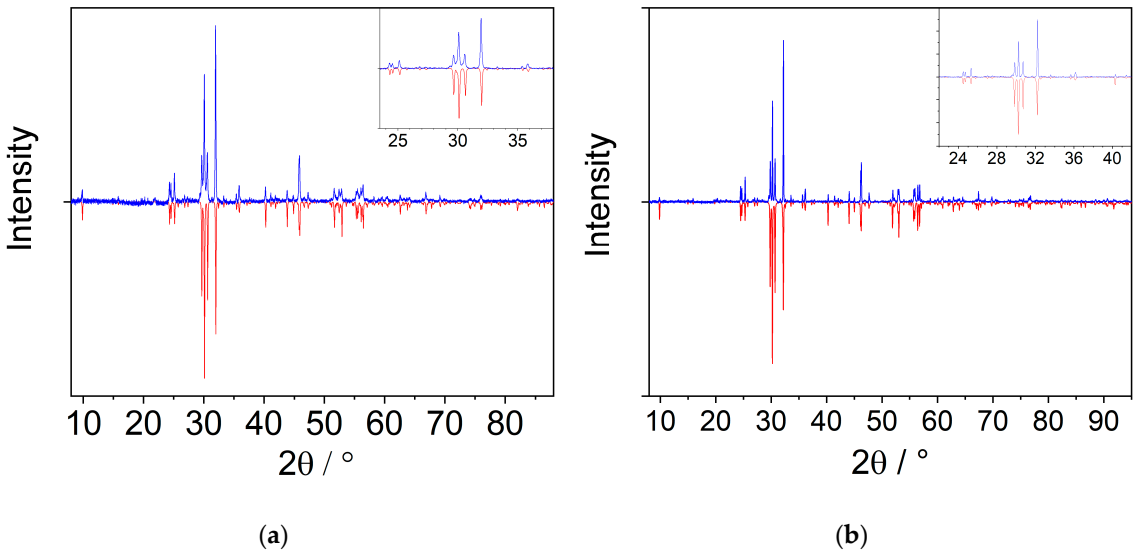

Figure A2. Measured (*blue*) and corresponding simulated (*red*) powder X-ray pattern of $EuSb_2O_4Br$ (**a**) and $TbSb_2O_4Br$ (**b**). While a high accordance of the measured and calculated reflection positions is given, texture effects probably due to the crystal habit generate visible differences in the relative intensities.

Table A5. Components and the average time of the multi-exponential decays reported in the manuscript. For the single-exponential decays, the fitted lifetime is reported as only the average value.

Sample	λ_{ex}/nm	λ_{em}/nm	A_1	τ_1/s	A_2	τ_2/s	τ_{avg}/s
$TbSb_2O_4Br:Eu^{3+}$	257	611	34.11	3.08×10^{-3}	65.89	1.09×10^{-3}	2.3×10^{-3}
	464	611					0.8×10^{-3}
	483	541					12.3×10^{-6}
$GdSb_2O_4Br:Eu^{3+}$	257	611	22.88	4.12×10^{-3}	77.12	1.04×10^{-3}	3.5×10^{-3}
	464	611	33.45	2.87×10^{-3}	66.55	7.74×10^{-4}	2.1×10^{-3}
	393	611	64.87	9.06×10^{-4}	35.13	4.65×10^{-3}	3.6×10^{-3}
$TbSb_2O_4Br$	483	541	22.54	1.39×10^{-4}	74.46	2.74×10^{-4}	0.25×10^{-3}

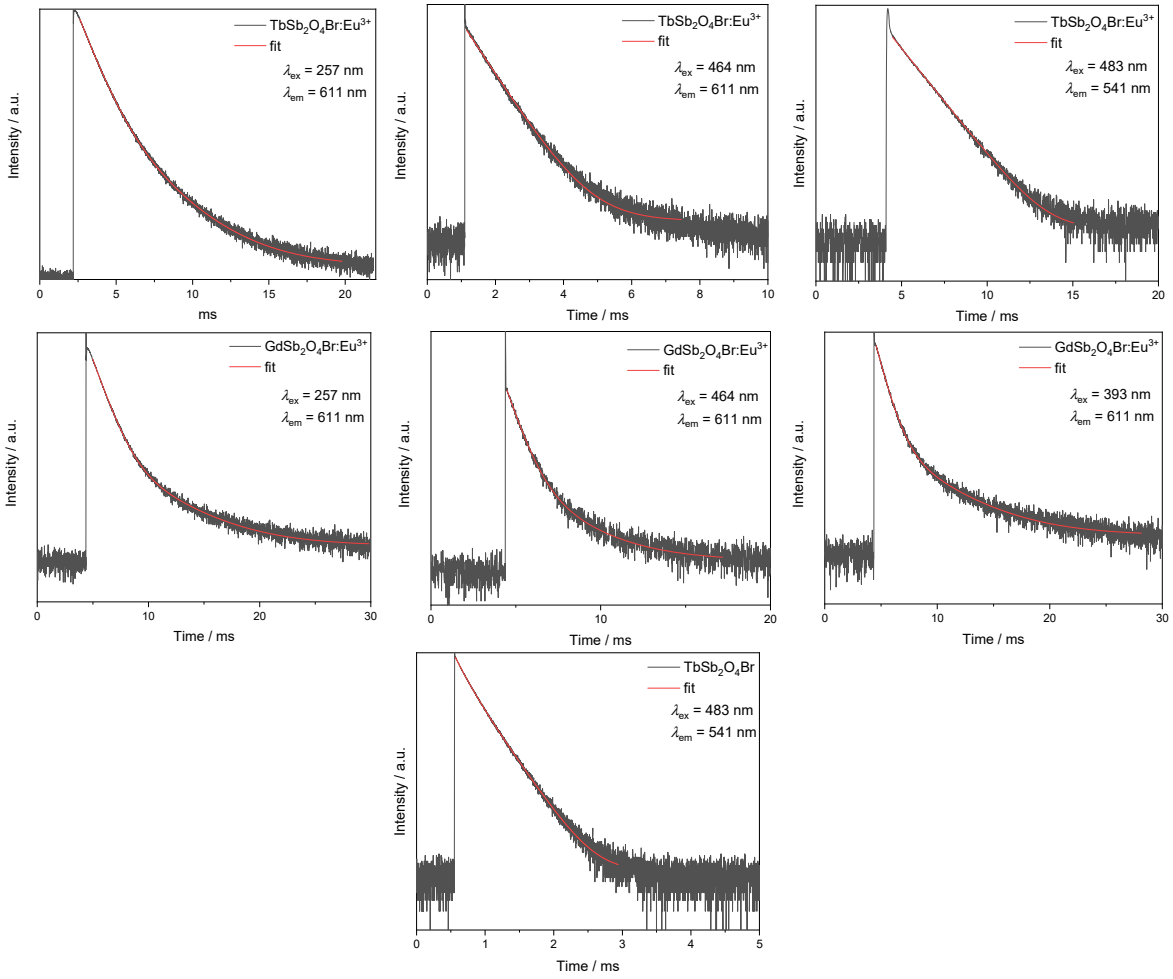

Figure A3. Intensity decay curves as measured (black) and fitted decay curves (red).

References

1. Ledderboge, F.; Nowak, J.; Massonne, H.-J.; Förg, K.; Höppe, H.A.; Schleid, T. High-pressure investigations of yttrium(III) oxoarsenate(V): Crystal structure and luminescence properties of Eu^{3+}-doped scheelite-type $Y[AsO_4]$ from xenotime-type precursors. *J. Solid State Chem.* **2018**, *263*, 65–71. [CrossRef]
2. Siqueira, K.P.F.; Lima, P.P.; Ferreira, R.A.S.; Carlos, L.D.; Bittar, E.M.; Granado, E.; González, J.C.; Abelenda, A.; Moreira, R.L.; Dias, A. Lanthanide Orthoantimonate Light Emitters: Structural, Vibrational, and Optical Properties. *Chem. Mater.* **2014**, *26*, 6351–6360. [CrossRef]

3. Li, C.; Hou, Z.; Zhang, C.; Yang, P.; Li, G.; Xu, Z.; Fan, Y.; Lin, J. Controlled Synthesis of Ln^{3+} (Ln = Tb, Eu, Dy) and V^{5+} Ion-Doped YPO_4 Nano-/Microstructures with Tunable Luminescent Colors. *Chem. Mater.* **2009**, *21*, 4598–4607. [CrossRef]
4. Bühler, G.; Feldmann, C. Microwave-assisted synthesis of luminescent $LaPO_4$:Ce,Tb nanocrystals in ionic liquids. *Angew. Chem. Int. Ed.* **2006**, *45*, 4864–4867. [CrossRef]
5. Dieke, G.H. *Spectra and Energy Levels of Rare Earth Ions in Crystals*; Interscience Publishers—John Wiley & Sons: New York, NY, USA, 1968.
6. Binnemans, K. Interpretation of europium(III) spectra. *Coord. Chem. Rev.* **2015**, *295*, 1–45. [CrossRef]
7. Deng, T.; Yan, S.; Hu, J. A novel narrow band UV-B emitting phosphor-YPO_4:Sb^{3+},Gd^{3+}. *J. Rare Earths* **2016**, *34*, 137–142. [CrossRef]
8. Ben Hamida, M.; Warns, C.; Wickleder, M.S. Syntheses and Crystal Structures of $RE_2As_4O_9$ (RE = Nd, Sm): Oxo-Arsenates(III) according to $RE_4(As_2O_5)_2(As_4O_8)$ Exhibiting the Cyclic $As_4O_8^{4-}$ Anion. *Z. Naturforsch.* **2005**, *60b*, 1219–1223. [CrossRef]
9. Kang, D.-H.; Schleid, T. $Sm_2As_4O_9$: Ein ungewöhnliches Samarium(III)-Oxoarsenat(III) gemäß $Sm_4[As_2O_5]_2[As_4O_8]$. *Z. Anorg. Allg. Chem.* **2006**, *632*, 91–96. [CrossRef]
10. Metzger, S.J.; Heymann, G.; Huppertz, H.; Schleid, T. La[AsO_3]: Lanthanum Oxoarsenate(III) with K[ClO_3]-Type Crystal Structure. *Z. Anorg. Allg. Chem.* **2012**, *638*, 1119–1122. [CrossRef]
11. Ledderboge, F.; Metzger, S.J.; Heymann, G.; Huppertz, H.; Schleid, T. Dimorphic cerium(III) oxoarsenate(III) Ce[AsO_3]. *Solid State Sci.* **2014**, *37*, 164–169. [CrossRef]
12. Goerigk, F.C.; Schander, S.; Hamida, M.B.; Kang, D.-H.; Ledderboge, F.; Wickleder, M.S.; Schleid, T. Die monoklinen Seltenerdmetall(III)-Chlorid-Oxidoarsenate(III) mit der Zusammensetzung $SE_5Cl_3[AsO_3]_4$ (SE = La – Nd, Sm). *Z. Naturforsch.* **2019**, *74b*, 497–506. [CrossRef]
13. Ben Hamida, M.; Wickleder, M.S. $Nd_5(AsO_3)_4Cl_3$: The First Oxo-Arsenate(III)-Chloride of the Lanthanides. *Z. Anorg. Allg. Chem.* **2006**, *632*, 2195–2197. [CrossRef]
14. Goerigk, F.C.; Schleid, T.; Schander, S.; Wickleder, M. The Triclinic Lanthanoid(III) Halide Oxidoarsenates(III) $Sm_3Cl_2[As_2O_5][AsO_3]$ and $Tm_3Br_2[As_2O_5][AsO_3]$. *Z. Anorg. Allg. Chem.* **2020**, *646*, 985–991. [CrossRef]
15. Kang, D.-H.; Schleid, T. $La_3OCl[AsO_3]_2$: Ein Lanthan-Oxidchlorid-Oxoarsenat(III) mit "Lone-Pair"-Kanalstruktur. *Z. Anorg. Allg. Chem.* **2007**, *633*, 1205–1210. [CrossRef]
16. Yahia, H.B.; Pöttgen, R.; Rodewald, U.C. Crystal Structure of $La_3OBr[AsO_3]_2$. *Z. Naturforsch.* **2010**, *65*, 1289–1292. [CrossRef]
17. Yahia, H.B.; Rodewald, U.C.; Pöttgen, R. Non-centrosymmetric $Ce_3OCl[AsO_3]_2$. *Z. Naturforsch.* **2009**, *64b*, 896–900. [CrossRef]
18. Kang, D.-H.; Schleid, T. $Ce_5Cl_3[AsO_3]_4$: The Second Chloride Oxoarsenate(III) of the Lanthanides, but the First One with Proper Crystallography. *Z. Kristallogr.* **2007**, *25*, 98.
19. Ok, K.M.; Gittens, A.; Zhang, L.; Halasyamani, P.S. Synthesis, structure and characterization of two new antimony oxides – $LaSb_3O_9$ and $LaSb_5O_{12}$: Formation of $LaSb_5O_{12}$ from the reaction of $LaSb_3O_9$ with Sb_2O_3. *J. Mater. Chem.* **2004**, *14*, 116–120. [CrossRef]
20. Marcano, C.M.; Rasines, I.; Vegas, A.; Otero-Diaz, L.C. Crystal Growth and Crystal Structure of $Gd_3Sb_5O_{12}$: A New Relation between the ccp and the Mn_5Si_3 and Apatite Structures. *Z. Anorg. Allg. Chem.* **1987**, *555*, 176–182. [CrossRef]
21. Cascales, C.; Marcano, C.M.; Rasines, I.; Fernández, F.; Sáez-Puche, R. Synthesis and characterization of $R_3Sb_5O_{12}$ (R = Nd, Sm Gd and Yb). *J. Less-Common Met.* **1989**, *149*, 63–66. [CrossRef]
22. Garcia Casado, P.; Mendiola, A.; Rasines, I. Preparation and crystal data of cerium antimony(III) trioxide. *Inorg. Chem.* **1982**, *21*, 2902–2903. [CrossRef]
23. Fernández, F.; Sáez-Puche, R.; Cascales, C.; Marcano, C.M.; Rasines, I. X-ray diffraction data and magnetic properties of the oxides $R_3Sb_5O_{12}$ (R = Pr, Nd, Sm, Eu, Gd, Yb). *J. Phys. Chem. Solids* **1989**, *50*, 871–875. [CrossRef]
24. Gukalova, A.G.; Tsejtlin, M.N. Crystal structure of lanthanum fluoroantimonite $La_5Sb_4O_{12}F_3$. *Kristallografiya* **1988**, *33*, 499–501.
25. Goerigk, F.C. Synthese und Charakterisierung von Seltenerdmetall-Oxidoarsenaten und -antimonaten, sowie deren Anwendungsbezug. Ph.D. Thesis, University of Stuttgart, Stuttgart, Germany, 2021. in preparation.
26. Goerigk, F.C.; Schleid, T. Composition and Crystal Structure of $SmSb_2O_4Cl$ Revisited—And the Analogy of $Sm_{1.5}Sb_{1.5}O_4Br$. *Z. Anorg. Allg. Chem.* **2019**, *645*, 1079–1084. [CrossRef]

27. Schmidt, M.; Oppermann, H.; Hennig, C.; Henn, R.W.; Gmelin, E.; Söger, N.; Binnewies, M. Untersuchungen zu Bismutseltenerdoxidhalogeniden der Zusammensetzung Bi_2SEO_4X (X = Cl, Br, I). *Z. Anorg. Allg. Chem.* **2000**, *626*, 125–135. [CrossRef]
28. Schmidt, M.; Oppermann, H. Synthese und Kristallstruktur von Bi_2ErO_4I. *Z. Anorg. Allg. Chem.* **1999**, *625*, 544–546. [CrossRef]
29. Aurivillius, B. Crystal structure of $NdBi_5O_8Cl_2$. Single crystal investigations on Bi_3O_4Br and $Bi_{12}O_{17}Cl_2$. *Chem. Scr.* **1984**, *24*, 125–129.
30. Hahn, F. STOE X-AREA. In *Software for Single-Crystal X-Ray Diffraction*; Stoe & Cie GmbH: Darmstadt, Germany, 2018.
31. Sheldrick, G.M. Crystal Structure Refinement with SHELXL. *Acta Crystallogr.* **2015**, *71*, 3–8. [CrossRef]
32. Sheldrick, G.M. *SHELX-97 Program Package for Single-Crystal Structure Solution and Refinement of X-Ray Diffraction Data*; University of Göttingen: Göttingen, Germany, 1997.
33. Rodriguez-Carvaja, J. Recent advances in magnetic structure determination by neutron powder diffraction. *Physica B.* **1993**, *192*, 55–69. [CrossRef]
34. Rodriguez-Carvajal, J. Fullprof Suite. Crystallographic tools for Rietveld, profile matching & integrated intensity refinements of X-Ray and/or neutron data. *Phys. B* **1995**, *55*, 192.
35. Roisnel, T.; Rodriguez-Carvajal, J. WinPLOTR: A Windows tool for powder diffraction patterns analysis. *Mater. Sci. Forum* **1999**, *378*, 118–123. [CrossRef]
36. Le Bail, A. Whole powder pattern decomposition methods and applications: A retrospection. *Powder Diffr.* **2005**, *20*, 316–326. [CrossRef]
37. Pouchou, J.-L.; Pichoir, F. A new model for quantitative X-ray microanalysis. *Rech. Aerosp.* **1984**, *3*, 167–192.
38. Pouchou, J.-L.; Pichoir, F. Quantitative Analysis of Homogeneous or Stratified Microvolumes Applying the Model "PaP". In *Electron Probe Quantitation*; Heinrich, K.F.J., Newbury, D.E., Eds.; Plenum Press: New York, NY, USA, 1991; pp. 31–75.
39. *PeakSight: CAMECA*; Société par Actions Simplifiée (SAS): Gennevilliers, France, 2019.
40. McCarthy, G.J. Crystal data on C-type terbium sesquioxide (Tb_2O_3). *J. Appl. Crystallogr.* **1971**, *4*, 399–400. [CrossRef]
41. Hubbert-Paletta, E.; Müller-Buschbaum, H. Röntgenographische Untersuchung an Einkristallen von monoklinem Tb_2O_3. *Z. Anorg. Allg. Chem.* **1968**, *363*, 145–150. [CrossRef]
42. Kohlmann, H.; Hein, C.; Kautenburger, R.; Hansen, T.C.; Ritter, C.; Doyle, S. Crystal structure of monoclinic samarium and cubic europium sesquioxides and bound coherent neutron scattering lengths of the isotopes ^{154}Sm and ^{153}Eu. *Z. Kristallogr.* **2016**, *231*, 517–523. [CrossRef]
43. Yakel, H.L. A refinement of the crystal structure of monoclinic europium sesquioxide. *Acta Crystallogr.* **1979**, *B 35*, 564–569. [CrossRef]
44. Pires, A.M.; Davolos, M.R.; Paiva-Santos, C.O.; Stucchi, E.B.; Flor, J. New X-ray powder diffraction data and Rietveld refinement for Gd_2O_3 monodispersed fine spherical particles. *J. Solid State Chem.* **2003**, *171*, 420–423. [CrossRef]
45. Atou, T.; Kusaba, K.; Fukuoka, K.; Kikuchi, M.; Syono, Y. Shock-induced phase transition of M_2O_3 (M = Sc, Y, Sm, Gd, and In-type compounds. *J. Solid State Chem.* **1990**, *89*, 378–384. [CrossRef]
46. Svensson, C. The crystal structure of orthorhombic antimony trioxide, Sb_2O_3. *Acta Crystallogr.* **1974**, *B 30*, 458–461. [CrossRef]
47. Svensson, C. Refinement of the crystal structure of cubic antimony trioxide, Sb_2O_3. *Acta Crystallogr.* **1975**, *B 31*, 2016–2018. [CrossRef]
48. Charkin, D.O.; Zitzer, S.; Greiner, S.; Dorofeev, S.G.; Olenev, A.V.; Berdonosov, P.S.; Schleid, T.; Dolgikh, V.A. Synthesis, Structures, and Luminescent Properties of Sodium Rare-Earth Metal(III) Chloride Oxotellurates(IV), $Na_2Ln_3Cl_3[TeO_3]_4$ (Ln = Sm, Eu, Gd, Tb, Dy, and Ho). *Z. Anorg. Allg. Chem.* **2017**, *643*, 1654–1660. [CrossRef]
49. Zitzer, S.; Schleifenbaum, F.; Schleid, T. $Na_2Y_3Cl_3[TeO_3]_4$: Synthesis, Crystal Structure and Spectroscopic Properties of the Bulk Material and its Luminescent Eu^{3+}-doped Samples. *Z. Naturforsch.* **2014**, *69b*, 150–158. [CrossRef]
50. Greiner, S.; Zitzer, S.; Strobel, S.; Berdonosov, P.S.; Schleid, T. The complete series of sodium rare-earth metal(III) chloride oxotellurates(IV) $Na_2RE_3Cl_3[TeO_3]_4$ (RE = Y, La–Nd, Sm–Lu). *Z. Kristallogr.* **2020**, *235*, 341–352. [CrossRef]

51. Edstrand, M.; Brodersen, R.; Sillén, L.G.; Linnasalmi, A.; Laukkanen, P. On the Crystal Structure of the Antimony Oxychloride $Sb_4O_5Cl_2$ and Isomorphous Oxybromide. *Acta Chem. Scand.* **1947**, *1*, 178–203. [CrossRef]
52. Mayerová, Z.; Johnsson, M.; Lidin, S. The structure of onoratoite, $Sb_8O_{11}X_2$ (X = Cl, Br) revisited. *Solid State Sci.* **2006**, *8*, 849–854. [CrossRef]
53. Lissner, F.; Schleid, T. $Sb_8O_{11}Br_2$: Ein sauerstoffreiches Antimon(III)-Oxidbromid. *Z. Kristallogr.* **2001**, *18*, 157.
54. Yu, Q.; Zeng, H.; Liu, Z.; Ren, J.; Chen, G.; Wang, Z.; Sun, L. Novel Sb^{3+}/Eu^{3+} Co-doped phosphate luminescent glasses with adjustable emission. *J. Alloys Compd.* **2014**, *590*, 92–95. [CrossRef]
55. Zhu, C.; Zhang, X.; Ma, H.; Timlin, C. Sb-, Dy-, and Eu-doped oxyfluoride silicate glasses for light emitting diodes. *J. Alloys Compd.* **2015**, *647*, 880–885. [CrossRef]
56. Hui, Y.; Zhao, Y.; Zhao, S.; Gu, L.; Fan, X.; Zhu, L.; Zou, B.; Wang, Y.; Cao, X. Fluorescence of Eu3+ as a probe of phase transformation of zirconia. *J. Alloys Compd.* **2013**, *573*, 177–181. [CrossRef]
57. Hoefdraad, H.E. The charge-transfer absorption band of Eu^{3+} in oxides. *J. Solid State Chem.* **1975**, *15*, 175–177. [CrossRef]
58. Dorenbos, P. Journal of Physics: Condensed Matter Systematic behaviour in trivalent lanthanide charge transfer energies. *J. Phys. Condens. Matter* **2003**, *15*, 8417–8434. [CrossRef]
59. Shi, X.; Li, J.-G.; Zhu, Q.; Li, X.; Sun, X. Hydrothermal assisted synthesis and photoluminescence of $(Y_{1-x}Eu_x)_2WO_6$ red phosphors. *J. Alloys Compd.* **2017**, *695*, 1984–1992. [CrossRef]
60. Reisfeld, R.; Zigansky, E.; Gaft, M. Europium probe for estimation of site symmetry in glass films, glasses and crystals. *Mol. Phys.* **2004**, *102*, 1319–1330. [CrossRef]
61. Avella, F.J.; Sovers, O.J.; Wiggins, C.S. Rare Earth Cathodoluminescence in $InBO_3$ and Related Orthoborates. *J. Electrochem. Soc.* **1967**, *114*, 613. [CrossRef]
62. Sá Ferreira, R.A.; Nobre, S.S.; Granadeiro, C.M.; Nogueira, H.I.S.; Carlos, L.D.; Malta, O.L. A theoretical interpretation of the abnormal $5D^0 \rightarrow 7F^4$ intensity based on the Eu^{3+} local coordination in the $Na_9[EuW_{10}O_{36}]\cdot 14H_2O$ polyoxometalate. *J. Lumin.* **2006**, *121*, 561–567. [CrossRef]
63. Zmojda, J.; Kochanowicz, M.; Miluski, P.; Baranowska, A.; Pisarski, W.A.; Pisarska, J.; Jadach, R.; Sitarz, M.; Dorosz, D. Optical Characterization of Nano- and Microcrystals of $EuPO_4$ Created by One-Step Synthesis of Antimony-Germanate-Silicate Glass Modified by P_2O_5. *Materials* **2017**, *10*, 1059. [CrossRef]